GEORG-AUGUST-UNIVERSITÄT
GÖTTINGEN

Fakultät für
Physik

Master's Thesis

Monte-Carlo-Validierung und Analyse neuronaler Netze für die Messung von $t\bar{t}V$-Prozessen bei 13 TeV

Towards the Measurement of $t\bar{t}V$ Processes at 13 TeV – Monte Carlo Validation and Neural Network Analysis

prepared by

Konstantin Lehmann

from Hamburg

at the II. Physikalisches Institut

Thesis number: II.Physik-UniGö-MSc-2016/02

Thesis period: 16th October 2015 until 15th April 2016

First referee: Prof. Dr. Arnulf Quadt

Second referee: Prof. Dr. Stanley Lai

Abstract

For the last 20 years, the top quark has been examined in detail. While some properties were experimentally determined, the third component of the top quark's weak isospin T_t^3 has never been measured directly. At the LHC, the production of a top quark pair and an associated Z boson ($t\bar{t}Z$ process) is sensitive to T_t^3. In order to detect this process, precise Monte Carlo (MC) simulations are compulsory. In this thesis, various simulations of $t\bar{t}Z$ processes are inspected for consistency. To ensure accurate modelling, different MC generators and PDFs are compared. Solid agreement is found suggesting consistent MC production. Thereafter, studies towards a first $t\bar{t}Z$ measurement at 13 TeV in the 2ℓOS final state channel are presented. Feed-forward neural networks are employed to separate signal from background processes. In particular, the influence of the network structure on signal discrimination is investigated.

Zusammenfassung

Seit seiner Entdeckung vor 20 Jahren wurde das Top-Quark intensiv untersucht. Viele seiner Eigenschaften wurden experimentell bestimmt, doch die dritte Komponente des schwachen Isospins des Top-Quarks T_t^3 ist noch nicht direkt gemessen worden. Am LHC ist die Produktion eines Top-Quark Paares und eines assoziierten Z Bosons ($t\bar{t}Z$-Prozess) sensitiv auf T_t^3. Um diesen Prozess nachzuweisen sind präzise Monte-Carlo-Simulationen (MC-Simulationen) unerlässlich. In dieser Arbeit werden Simulationen von $t\bar{t}Z$-Prozessen auf Fehler geprüft. Verschiedene MC-Generatoren und PDFs werden verglichen, um eine genaue Modellierung zu gewährleisten. Dass sie gut übereinstimmen, spricht für konsistente MC-Produktion. Danach werden Studien für eine spätere Messung des $t\bar{t}Z$-Prozesses bei 13 TeV im 2ℓOS-Kanal vorgestellt. Neuronale „Feed-Forward"-Netze werden benutzt, um Signal- von Untergrundprozessen zu trennen. Insbesondere der Einfluss der Netzwerkstruktur auf die Signaltrennung wird untersucht.

Contents

1. Introduction

In the early 20th century, one single observation was often sufficient to discover a new particle. Evidence for the muon, for example, was reported based on one 7 cm long ionisation track in a cloud chamber [1]. Today, in contrast, collaborations at high-energy experiments often use complicated simulations to perform their analyses. They process plenty of data in order to support a hypothesis. Why are contemporary analyses so substantially different from the earlier, more basic approaches? Why did we diverge from straightforward techniques?

The main reason is the different treatment of backgrounds. When Street and Stevenson discovered the muon in 1937, they interpreted 1000 photographs. They knew exactly which signatures backgrounds would yield in the detector. Protons and electrons would ionise less and the proton would be deflected in the other direction. Thus, they could tell the muon apart.

In the course of time, particle colliders were built to artificially produce particles with higher masses. Bottom quark pairs, for instance, were discovered by detecting the decay into muons at fixed-target experiments [2]. The setup was not designed to make backgrounds easily identifiable. Instead, the experimenters knew that background events would steadily decline with increasing invariant muon mass. When they observed a bump in this continuous spectrum, they had found a resonant state. In this approach, the background treatment is fundamentally different. The background-only hypothesis can be excluded statistically by exploiting knowledge of the background[1].

Nowadays, collisions at particle colliders obtain higher energies and produce more final-state particles. This often causes signal and background signatures to become more complex and more elaborate techniques are needed to filter the signal. Therefore, it is difficult to estimate analytically, how many diverse background events contaminate the signal selection. To solve this problem, Monte Carlo (MC) simulations are employed. They use statistical methods to numerically model fundamental particle interactions in the expected signal and background. These simulations are then used to assess how much background compromises a measurement.

[1] Incidentally, one of the Higgs boson discovery channels ($H \to \gamma\gamma$) used this technique in 2012.

MC generators are very sophisticated tools. They incorporate both predictions from quantum field theories and models of analytically inaccessible areas. Although the generators are remarkably elaborate, they cannot reach universal precision. Consequently, it is crucial to make sure that their output correctly models theoretical predictions.

The main part of this thesis is dedicated to validating the modelling of MC generators. Simulations of $t\bar{t}$ production in association with a Z boson ($t\bar{t}Z$) are analysed and different settings towards Run 2 are compared. All these studies are motivated by the prospect of precise $t\bar{t}V$ measurements[2].

Chapter 2 gives an introduction to the Standard Model of particle physics. The focus lies on physics related to the top quark and especially associated $t\bar{t}V$ production. Thereafter, the simulation steps of MC generators are summarised in chapter 3 before chapter 4 gives a short overview of the "A Toroidal LHC ApparatuS" (ATLAS) experiment at the "Large Hadron Collider" (LHC). The above-mentioned validation of MC simulations is presented in chapter 5. First studies towards $t\bar{t}V$ signal and background discrimination are outlined in chapter 6 applying multivariate analysis (MVA) techniques. Chapter 7 summarises the various aspects of this thesis and concludes.

[2]The abbreviation $t\bar{t}V$ combines both $t\bar{t}Z$ and $t\bar{t}W$ processes, a $t\bar{t}$ pair and an associated Z or W boson.

2. Physics at the LHC

The concept of discrete, indivisible matter particles dates back to ancient times. Philosophers speculated that this smallest constituent of matter, the "atom", could be assembled to any material. While this had been a philosophical concept at first, scientific experiments supported this assumption from the late 19th century on.

When physicists started to observe many new particles at high energy experiments in the 1950s, they concluded that not all of them were elementary. As a consequence, the Standard Model of particle physics (SM) was developed. It arranged the particles and forces in such a way that many of the detected resonances were reduced to more fundamental particles. The following section gives an overview of the SM explaining its underlying concept, electroweak unification and in more detail the physics related to the top quark.

2.1. Overview of the Standard Model

Particles are split up into two distinct groups according to their spin quantum number. Fermions with half-integer spin are matter particles and bosons with integer spin are interaction particles. The three left columns in Figure 2.1 show fermions and the five boxes on the right represent bosons. Fermions can be further subdivided into leptons (two top rows) and quarks (two bottom rows). The three fermions in one row have the same quantum numbers and only differ in their masses. They are displayed in increasing order of mass. The columns are called generations or families. All fermions can be assigned a helicity defined as the projection of spin onto the direction of propagation. In the limit of a massless particle, helicity is equal to chirality. The chirality is a Lorentz invariant property and divides fermions into left-chiral and right-chiral states.

The two left-handed leptons in the same column form a pair of weak-isospin partners, eg. electron neutrino ν_e (with the third component of the weak isospin $T^3 = \frac{1}{2}$) and electron e^- ($T^3 = -\frac{1}{2}$). In the same manner, the up quark's weak-isospin partner is the down quark. Right-handed fermions, conversely, have no isospin relating them. The electron and its heavier duplicates, the muon and tau lepton,

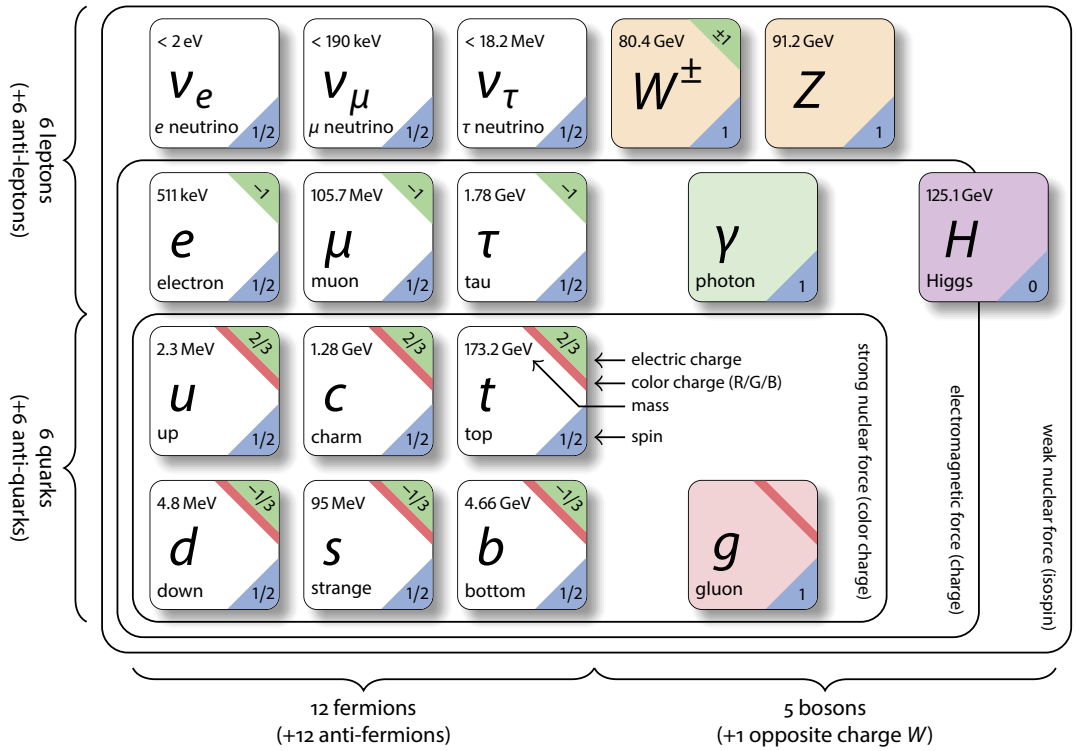

Figure 2.1.: Fermions and bosons in the Standard Model of particle physics. The masses are taken from Ref. [3] including updates from 2015.

have an electric charge of -1 in units of the elementary charge[1], while neutrinos have no charge. Quarks also carry electric charge, namely $+\frac{2}{3}$ for up-type and $-\frac{1}{3}$ for down-type quarks. As opposed to leptons, quarks have another property called colour charge, which makes them interact by means of the strong force. This interaction prevents the occurrence of free colour charges at low energies. Therefore, quarks form hadrons in a way that the net colour charge vanishes. A proton, for example, is composed of one down quark and two up quarks.

In relativistic quantum mechanics, fermions are described by the Dirac equation. The solutions have eigenvalues with positive or negative energies implying that for every particle there is an antiparticle with the same mass, but opposite quantum numbers. For instance, the antiparticle of the electron e^- is the positron e^+ with positive electric charge.

The fundamental forces are derived from gauge symmetries in the SM. The idea is to construct a Lagrangian density describing physical particles as fields and to demand it to be invariant under local gauge transformations. The invariance can be accomplished by rewriting derivatives and introducing interaction fields corre-

[1]Elementary electric charge $e \approx 1.6 \cdot 10^{-19}$ C [3].

sponding to the gauge bosons. This is a predictive way of introducing interactions just by demanding local gauge invariance. In case of the SM, the Lagrangian is invariant under the gauge groups $SU(3) \times SU(2) \times U(1)$, which describe the strong interaction ($SU(3)$) and the unification of the weak and electromagnetic interaction ($SU(2) \times U(1)$).

The detailed mathematical description shows which particles gauge bosons couple to. Eight gluons g, which only differ in their combination of colour and anti-colour charge, are the gauge bosons of the strong interaction (Quantum Chromodynamics, QCD). They couple to all particles with colour charge, i.e. to quarks and to themselves. The extensive self-coupling is responsible for the fact that QCD is very strong at low energies compared to other interactions. This strength entails that colour charges cannot be observed freely, but are confined instead.

The gauge boson of the electromagnetic force is called photon γ and couples to all particles with electric charge. The weak interaction is mediated by the W^+, W^- and Z bosons, which couple to all fermions and themselves. While the neutral currents (γ and Z) do not change fermion flavour, the $W^\pm$ bosons couple to the two corresponding weak-isospin partners[2] and therefore change flavour.

When the SM was developed, it reduced the massive number of observed particles to a small set of fundamental particles and described their interactions with three forces. This was a great success on its own. In addition, the SM also predicted new particles and even their approximate masses. When these particles, i.e. the W, Z boson and the top quark, were discovered one after another, it gave stronger confirmation of the SM. Finally, the discovery of the Higgs boson in 2012 [4, 5] confirmed that the Brout-Englert-Higgs (BEH) mechanism [6, 7] gives mass to elementary particles and verified yet another assumption.

Despite its reliable predictions, the SM fails to explain some phenomena in our universe. For instance, it completely disregards gravitational interactions. This might be reasonable on small scales, but everyday-experience reveals that gravity is influential on large scales. Moreover, gravitational attraction between galactic centres and faraway stars is stronger than expected from calculations. This astronomical observation suggests that there might exist a still undetected kind of matter, often called dark matter. Many extensions of the SM, eg. supersymmetric models, include dark matter candidates in the form of weakly interacting massive particles.

Furthermore, the SM has some intrinsic flaws [8]. It needs 25 input variables to fit experimental data. For instance, all fermion masses and coupling constants are introduced this way. Although theory predictions match observed data well, the 25 free parameters suggest that there be a mechanism relating them. Moreover, the

[2]Note that this statement refers to weak interaction eigenstates. Section 2.2 reveals that quarks can also couple to quarks from other generations.

SM incorporates both matter and antimatter, but fails to explain why matter seems to exceed antimatter in our universe. Another issue is related to neutrinos. In the SM they are massless, but their oscillation between different flavour states [9, 10] implies that they have mass. In addition, there is also a point of a rather conceptual nature. The SM describes three generations of fermions and three interactions. The question arises, whether they can be reduced to one. In fact, the electromagnetic and weak interactions are unified as illustrated in the following section. It is desirable, however, to obtain a more fundamental description by harmonising them with the strong interaction. These and other questions are the main motivation of current research in particle physics.

2.2. Electroweak Unification

In the mid-nineteenth century, Maxwell described the two phenomena of electricity and magnetism in one unified theory. Following the same idea, also the electromagnetic and weak interactions can be harmonised to the electroweak theory. To unify the two forces, underlying mechanisms need to be established to compensate for their differences. The most striking inconsistencies are related to parity conservation and boson masses. While electromagnetism is purely symmetric and the photon is massless, the weak interaction treats left- and right-handed particles differently and has massive force carriers. This section outlines how these two issues are overcome to achieve electroweak unification.

In 1957, Wu discovered that parity conservation is violated in weak decays [11]. This implies that the vertex structure of the W boson is not purely vectorial, as originally proposed by Fermi. Electron helicity measurements in muon decays indicated that the weak, charged current maximally violates parity [12]. A measurement of the neutrino helicity [13] gave evidence that the vertex has a vector-axial vector (V-A) structure

$$\frac{-ig_W}{2\sqrt{2}}(\underbrace{\gamma^\mu}_{\text{V}} - \underbrace{\gamma^\mu\gamma^5}_{\text{A}}),$$

where γ^μ are the Dirac matrices and $\gamma^5 = i\gamma^0\gamma^1\gamma^2\gamma^3$ is the product of them. The electromagnetic interaction preserves parity and is fundamentally different from the weak one in this regard. This issue is solved by absorbing the structure of the

coupling into the fermion spinor. One defines

$$P_L = \frac{1-\gamma^5}{2}$$
$$P_R = \frac{1+\gamma^5}{2}$$

to be projection operators to left- and right-handed fermion states. Thus, the weak force can be interpreted as a vectorial coupling, that distinguishes between left- and right-handed particles. This solves the first problem when unifying the two interactions.

To harmonise boson masses, a look at the electroweak $SU(2) \times U(1)$ symmetry group is necessary. This group has $3+1$ generators corresponding to the same number of gauge bosons, commonly denoted as W^1, W^2, W^3, B. At this point, the interaction between neutrinos and their weak-isospin partners is mediated by a combination of W^1 and W^2, but none of them can be identified with W^+ or W^-. In the same way, the B behaves very much like the photon but additionally couples to neutrinos. This is resolved by mixing the states in the following way:

$$\begin{pmatrix}\gamma\\ Z\end{pmatrix} = \begin{pmatrix}\cos\theta_W & \sin\theta_W\\ -\sin\theta_W & \cos\theta_W\end{pmatrix}\begin{pmatrix}B\\ W^3\end{pmatrix}$$
$$\begin{pmatrix}W^+\\ W^-\end{pmatrix} = \frac{1}{\sqrt{2}}\begin{pmatrix}-1 & i\\ -1 & -i\end{pmatrix}\begin{pmatrix}W^1\\ W^2\end{pmatrix}$$

The physical fields on the left-hand side are constructed by mixing the gauge fields. They correspond to the photon γ, Z boson and W bosons. The variable θ_W is the Weinberg angle, also called "electroweak mixing angle".

This very mixing does not only describe the couplings correctly, but also accounts for different gauge boson masses. After Glashow first suggested unifying both forces [14], Weinberg and Salam explained the different masses [15, 16] applying the BEH mechanism[3]. When generating gauge boson masses, the mixing with the Weinberg angle is responsible for both the Z boson to acquire more mass than the W and for the γ to stay massless.

After unification, the interaction of the Z boson is described by the Lagrangian

$$\mathcal{L}_Z = \frac{g_e}{2\sin\theta_W\cos\theta_W}\sum_{\substack{f=L_L,e_R,\\ Q_L,u_R,d_R}} Z_\mu \bar{f}\,(\underbrace{T_f^3 - 2Q_f\sin^2\theta_W}_{\text{vector}} - \underbrace{T_f^3\gamma^5}_{\text{axial vector}})\,\gamma^\mu f, \qquad (2.1)$$

[3]The BEH mechanism is a crucial part of the SM. However, it is not directly related to this work and therefore not discussed in full. More information about the BEH mechanism, Higgs potential and boson can be found in textbooks, e.g. [8].

where g_e is the electromagnetic coupling constant, $L_L = \begin{pmatrix} \nu_e \\ e^- \end{pmatrix}$ and $Q_L = \begin{pmatrix} u \\ d \end{pmatrix}$ are the weak-isospin doublets of the left-handed leptons and quarks[4]. The index R denotes right-handed isospin singlets, which by definition have a weak isospin of $T^3_{f_R} = 0$. Q_f stands for the electric charge of the fermion. Similarly, the leptonic interaction of the W boson can be written

$$\mathcal{L}_{W,\,\text{lept}} = \frac{g_e}{\sqrt{2} \cdot \sin\theta_W} \, W^+_\mu \, \left(\bar{\nu}_e, \bar{\nu}_\mu, \bar{\nu}_\tau\right)_L \, \gamma^\mu \begin{pmatrix} e^- \\ \mu^- \\ \tau^- \end{pmatrix}_L + \text{h.c.}$$

For interactions with quarks, another effect needs to be taken into account. The W boson does not only couple to one doublet, but also mixes generations. This feature was first described by Cabibbo [17], who suggested to add factors of $\sin\theta_C$ and $\cos\theta_C$ to the respective Lagrangians. At present, as three generations of quarks are known, a three-dimensional rotation matrix is needed. The unitary Cabibbo-Kobayashi-Maskawa (CKM) matrix[5] [18] describes the rotation between the mass eigenstates and the weak interaction eigenstates of down-type quarks (primed on the left-hand side)

$$\begin{pmatrix} d' \\ s' \\ b' \end{pmatrix} = \begin{pmatrix} V_{ud} & V_{us} & V_{ub} \\ V_{cd} & V_{cs} & V_{cb} \\ V_{td} & V_{ts} & V_{tb} \end{pmatrix} \begin{pmatrix} d \\ s \\ b \end{pmatrix}$$

The diagonal elements are close to one favouring couplings within a generation. In case of the top quark, the experimental value $|V_{tb}| = 1.021 \pm 0.032$ (combination by Ref. [3]) even lies above the theoretical constraints[6]. With the CKM matrix, the W coupling to quarks reads

$$\mathcal{L}_{W^\pm,\,\text{quarks}} = \frac{g_e}{\sqrt{2} \cdot \sin\theta_W} \, W^+_\mu \, \left(\bar{u},\, \bar{c},\, \bar{t}\right)_L \, \gamma^\mu V_{\text{CKM}} \begin{pmatrix} d \\ s \\ b \end{pmatrix}_L + \text{h.c.}$$

[4]For simplicity, only the first generation of particles is explicitly written out. Of course, the second and third generation couple equivalently.

[5]The CKM matrix can be parametrised with four parameters. These four parameters belong to the free SM input values mentioned in section 2.1.

[6]The CKM matrix is unitary. Hence, the sum of squared elements within a row must yield unity: $|V_{td}|^2 + |V_{ts}|^2 + |V_{tb}|^2 = 1$.

2.3. Top Quark

The top quark was first discovered by the CDF and DØ collaborations [19, 20] at the Fermilab laboratory in 1995. First assumptions of a third generation of particles had been made even before the charm quark (as the fourth quark) was discovered. With their suggestion of the CKM matrix, Kobayashi and Maskawa explained CP violation assuming the existence of the bottom and top quark. When in 1975 the τ lepton, and thereby the first third-generation particle was discovered [21], and two years later also the bottom quark [2], there was a strong indication for the existence of the top quark.

Two properties make the top quark interesting for measurements. It is the heaviest known elementary particle with $m_t = (173.34 \pm 0.76)$ GeV [22] and has a short decay time of approximately $0.5 \cdot 10^{-25}$ s [8]. As hadronisation occurs in the order of 10^{-23} s [23], the top quark decays before it forms hadrons. Therefore, its bare properties can be studied by analysing the decay products. Due to its high mass, it decays into an on-shell W^+ boson and a quark, almost exclusively a b quark. In this decay process, the top quark transfers its properties to its decay products and makes them accessible in measurements.

2.3.1. Production

The Tevatron and the LHC are the only two particle colliders which were[7] and are able to produce a significant number of top quarks. At both, $t\bar{t}$ pair production is the predominant process. The leading order (LO) diagrams are depicted in Figure 2.2. As protons and anti-protons were collided at Tevatron, $q\bar{q}$ annihilation mainly contributed to $t\bar{t}$ production, while for proton-proton collisions at the LHC gg fusion dominates. It contributes with about 90% at centre-of-mass energies of $\sqrt{s} = 14$ TeV [3].

At different centre-of-mass energies, the share in production mechanism shifts due to the momentum distributions inside the colliding protons [24]. Only two partons (one per colliding proton) participate in the hard scattering process. These partons do not carry all the proton momentum, but just a fraction x. To produce a top quark pair, an energy of at least $2m_t$ has to be available. In terms of momentum fractions x_1 and x_2, this condition reads $\hat{s} = x_1 x_2 s > 4m_t^2$.

The probability of a parton to carry a certain momentum fraction is expressed by parton distribution functions (PDFs) $f_i(x)$. The number of partons of type i with a momentum fraction between x and $x + \delta x$ is given by $f_i(x) \cdot \delta x$ [8]. Figure 2.3 shows PDFs for protons at the energy scale of $Q^2 = 30{,}000$ GeV$^2 \approx m_t^2$, which is commonly

[7] Last Tevatron collisions took place in 2011.

used for $t\bar{t}$ computations. Because QCD is non-perturbative at low energies, PDFs cannot be calculated from first principles but have to be measured. Important contributions were made by the HERA collider (1991-2007), which examined deep inelastic scattering of asymmetric electron (and positron) proton collisions.

The majority of top quarks are produced in pairs. At 13 TeV centre-of-mass energy, the cross section is

$$\sigma_{pp\to t\bar{t}} = 831.76^{+19.77}_{-29.20}(\text{scale})^{+35.06}_{-35.05}(\text{pdf}+\alpha_s)^{+23.18}_{-22.45}(m_t)\ \text{pb}$$

computed at next-to-next-to-leading order with the Top++2.0 program [27]. A top mass of $m_t = 172.5$ GeV was chosen and different PDFs were combined. Apart from pair creation, single top quarks are produced through the electroweak interaction. Three types of diagrams contribute at LO: an s-channel W boson decaying into $t\bar{b}$, t-channel W exchange between a b quark and another quark, and a b quark radiating off a W boson. While top and antitop quarks are equally produced in pair production, in the single production mode top quarks are preferably created with respect to antitop quarks at the LHC. Combining the three processes for top and antitop yields a cross section of

$$\sigma_{pp\to\text{single } t} = 216.99^{+6.62}_{-4.64}(\text{scale})^{+6.16}_{-6.16}(\text{pdf}+\alpha_s)^{+1.81}_{-1.81}(m_t)\ \text{pb}.$$

This value was calculated at next-to-leading order (NLO) with the Hathor2.1 program [28, 29] and the same top mass and PDFs as for pair production.

2.3.2. Decay

The top quark decays weakly into a W boson and a down-type quark. The respective elements of the CKM matrix determine with which probability each of the three quark flavours emerge. The value of $|V_{tb}|$ is large compared to the other entries $|V_{ts}|$ and $|V_{td}|$ and makes the vast majority of top quarks decay into W bosons and b quarks. These b quarks rapidly form hadrons and decay after covering a distance of a few millimetres on average. During this decay further particles are created, which are all together observed as jets in the detector.

The W boson decays into quarks and leptons (see Figure 2.4). Disregarding quark mixing for now, there are three lepton combinations and two quark combinations, which are lighter than the W boson. As quarks can be produced in three different colour states, the hadronic decay must be weighted with this factor. In conclusion, there are $3 + 3 \cdot 2 = 9$ combinations in total. In the lowest-order prediction, the W boson is approximately equally likely to decay into every possible combination of quarks and leptons. Thus it decays into quarks in $\frac{2}{3}$ and into leptons in $\frac{1}{3}$ of the

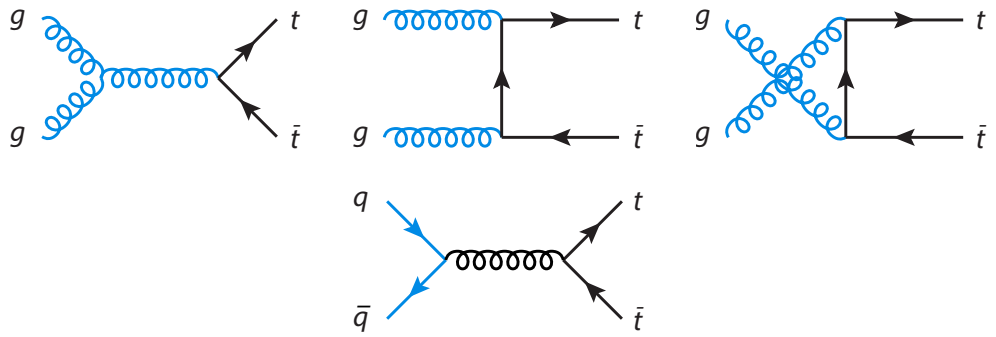

Figure 2.2.: LO $t\bar{t}$ pair production diagrams: Gluon fusion (top) and $q\bar{q}$ annihilation (bottom).

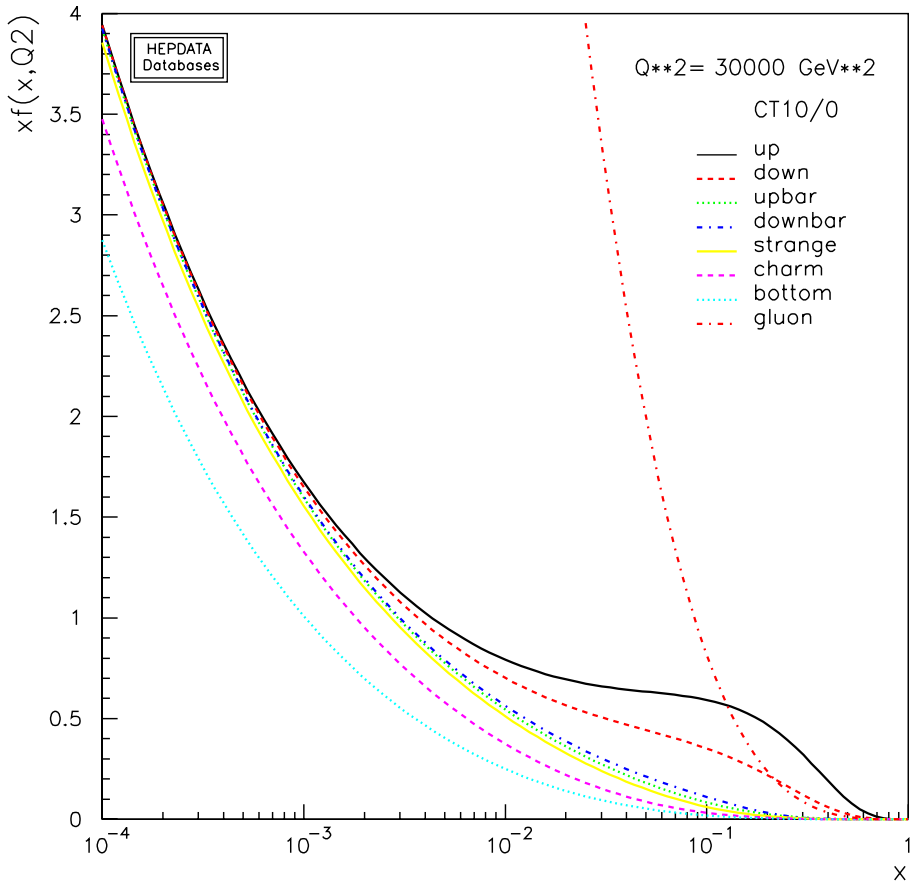

Figure 2.3.: Parton distribution functions for a proton at the energy scale of $Q^2 = 30{,}000$ GeV $\approx m_t^2$. The x-axis shows the momentum fraction x and the y-axis the momentum distribution function $x \cdot f_i(x)$. The plot is based on the PDF set CT10 [25]. This Figure was created with a tool provided by the Durham HepData Project [26].

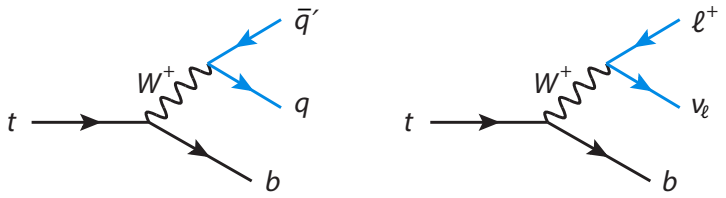

Figure 2.4.: Top quark decay. The top quark radiates off a W boson and turns into a b quark in most cases. The W boson decays further into a lepton-neutrino pair (left) or two quarks (right). This process happens equivalently for the $\bar{t}$ quark.

Decay mode	Decay particles from t	Decay particles from $\bar{t}$	Signature	Probability
all-hadronic	$b, q, \bar{q}'$	$\bar{b}, q'', \bar{q}'''$	6 jets	45.7%
lepton+jets	$b, q, \bar{q}'$ $b, \bar{\ell}, \nu_\ell$	$\bar{b}, \ell, \bar{\nu}_\ell$ $\bar{b}, q, \bar{q}'$	4 jets, 1 charged lepton	43.8%
dileptonic	$b, \bar{\ell}, \nu_\ell$	$\bar{b}, \ell', \bar{\nu}_{\ell'}$	2 jets, 2 charged leptons	10.5%

Table 2.1.: Decay channels of top quark pairs [3]. ℓ and $\bar{\ell}$ stand for negatively and positively charged leptons, respectively. Quarks are primed to indicate that they do not necessarily have the same flavour.

cases. Corrections come from quark mixing, phase space considerations and gluon radiation in hadronic decays, enhancing the quark yield.

The signature of a $t\bar{t}$ decay is determined by the decay of the W bosons. Combinatorially three signatures are possible, as outlined in Table 2.1. All-hadronic decays have a high branching ratio, but suffer from a low signal-over-background ratio. QCD processes cause a high multi-jet yield and result in a major background. Moreover, the jet resolution is imprecise compared to lepton resolution. In contrast, the dileptonic channel has two rather easily recognisable charged leptons[8], but suffers from a low branching ratio and a large missing transverse momentum from the neutrinos. Due to the missing information, the $t\bar{t}$ kinematics cannot unambiguously be reconstructed. The lepton+jets channel is somewhere in-between. It reduces the background with respect to the all-hadronic decay and still has higher statistics than the dileptonic decay channel.

[8]This statement is mostly valid for electrons and muons. Reconstruction of τ leptons is more delicate, because they decay before reaching the detector.

2.3.3. Couplings

In addition to the electroweak coupling, the top quark also couples to all other SM bosons. The interaction between the Higgs field and fermions is described by the Yukawa interaction. It is proportional to the fermion mass. Thus, the top quark, being the heaviest fermion, is very suitable to probe this interaction. The precise value of the top Yukawa coupling can set limits on new physics as no other SM variable [30]. Small variations in this coupling can change the Higgs mass and thus the Higgs potential drastically. If the value is such that the Higgs potential has a minimum at high energies, it would be unlikely that the universe had ended up in our actual, low energy-vacuum state. New physics would be needed below some energy scale to eliminate the high-energetic minimum of the Higgs potential and to account the present vacuum state. To make predictions about the energy scale of new physics, the top quark Yukawa coupling needs to be measured precisely.

Electromagnetic couplings to fermions give access to the electric charge, because the respective vertex factor depends linearly on it. At e^+e^--colliders the absolute value of quark charges could be measured through the cross section ratio $R(s) = \frac{\sigma(e^+e^- \to \text{hadrons})}{\sigma(e^+e^- \to \mu^+\mu^-)}$. But the top quark was inaccessible, since centre-of-mass energies were too low to produce the necessary quantity of top quark pairs. Although the exotic scenario of $q_t = -\frac{4}{3}e$ could be excluded [31], the direct measurement of the top quark charge is a major motivation for investigating its electromagnetic coupling.

In $t\bar{t}\gamma$ production, a photon can be radiated from a top quark, but also from all other charged particles participating in top quark production and decay. The interference terms of these processes are non-negligible [32] and the measurement of the $t\gamma$ coupling is not trivial. On the way to examining the coupling, the ATLAS collaboration recently published observation of the associated $t\bar{t}\gamma$ production [33].

When top quark pairs are produced in typical QCD processes, they couple to gluons. This interaction is suitable to investigate the strong coupling. Of particular interest is the detection of flavour changing neutral currents (FCNC), which are excluded by the SM at LO. They would make processes possible, in which a gluon converts an up or charm quark into a top quark. Only upper limits to FCNCs have been reported so far [34, 35].

Although the reconstruction of top quarks assumes the presence of the electroweak decay into W bosons, this very coupling is still subject to research. In the SM the Wtb vertex is left-handed and has no right-handed component. Hence, in the massless limit the b quark must be left-handed and the W boson has two helicity options. It has either left-handed or longitudinal helicity, while right-handed polarisation is excluded [36]. To assess this prediction and to find hints for anomalous couplings,

angular distributions of top quark decay products give some insight. However, all measurements agree with the SM prediction and set exclusion limits to anomalous couplings [37, 38].

The coupling of top quarks to Z bosons (tZ coupling) is also of major research interest. Similar to the gluon, FCNCs are suppressed in the SM and an excess would be an indication for new physics. The CMS collaboration sets limits of 0.07% on the top quark branching ratio to a Z boson and a light up-type quark [39]. Secondly, the tZ vertex gives access to the third component of the top quark's weak isospin as discussed in the next section.

2.4. $t\bar{t}W$ and $t\bar{t}Z$ Processes

The production of a top quark pair and an associated vector boson W or Z can yield further insights into electroweak couplings. Depending on the decay modes of the $t\bar{t}$ pair and vector boson, several final-state signatures occur as outlined in Table 2.2. Since some signatures overlap, $t\bar{t}W$ and $t\bar{t}Z$ are usually analysed simultaneously. Nevertheless, the main motivation for $t\bar{t}V$ analyses is the sensitivity to the weak isospin of the top quark in $t\bar{t}Z$ processes.

	$Z \to \ell\bar{\ell}$	$Z \to \nu\bar{\nu}$	$Z/W \to jj$	$W \to \ell\nu$
dileptonic	$4\ell\ 2j(2b)$	$2\ell\ 2j(2b)$	$2\ell\ 4j(2b)$	$3\ell\ 2j(2b)$
ℓ+jets	$3\ell\ 4j(2b)$	$1\ell\ 4j(2b)$	$1\ell\ 6j(2b)$	$2\ell\ 4j(2b)$
all-hadronic	$2\ell\ 6j(2b)$	$6j(2b)$	$8j(2b)$	$1\ell\ 6j(2b)$

Table 2.2.: Final-state signatures of $t\bar{t}V$ processes. Each row represents one $t\bar{t}$ decay mode and each column one vector boson decay. The jets and b-jets are denoted by j and b, leptons by ℓ. The sum of lepton charges is 0 or 1 in all cases, apart from the $t\bar{t}$ decay in the ℓ+jets channel combined with the leptonic W decay. In this case, the rare final state of two leptons with same sign can occur.

2.4.1. Motivation: tZ Coupling

In the SM, the top quark coupling to the Z boson is described by the Lagrangian density in eq. (2.1). Considering possible extensions to the SM [40], the Z boson interaction Lagrangian to the top quark can be written

$$\mathcal{L}_{t\bar{t}Z} = g_e \bar{u}(p_t) \left[\gamma^\mu (C_{1,V} + \gamma^5 C_{1,A}) + \frac{i\sigma^{\mu\nu} q_\nu}{M_Z} (C_{2,V} + i\gamma^5 C_{2,A}) \right] u(p_{\bar{t}}) Z_\mu$$

with $\sigma^{\mu\nu} = \frac{i}{2}[\gamma^\mu, \gamma^\nu]$ and $q_\nu = (p_t - p_{\bar{t}})_\nu$. The left term in the square brackets represents the SM vector and axial vector couplings with the coefficients $C_{1,V/A}$. Their SM values are given by

$$\begin{aligned} C_{1,V}^{SM} &= \frac{T_t^3 - 2Q_t \sin^2\theta_W}{2\sin\theta_W \cos\theta_W} \approx 0.24 \\ C_{1,A}^{SM} &= \frac{-T_t^3}{2\sin\theta_W \cos\theta_W} \approx -0.60 \end{aligned}$$

The variables $C_{2,V/A}$ parametrise tensor couplings, which are predicted to be non-existent in the SM.

The Lagrangian reveals that the tZ coupling depends on the weak mixing angle θ_W, the top quark charge Q_t and the third component of the top quark's weak isospin T_t^3. The electric charge of the top quark and the Weinberg angle are known to some precision and the unknown parameter is T_t^3. Thus, examining the tZ vertex allows to measure this parameter and to compare it to the SM expectation of $T_t^{3,SM} = +\frac{1}{2}$. While most other SM top quark properties have been confirmed, T_t^3 has never been directly determined experimentally.

The tZ coupling occurs seldom at the LHC. To probe this vertex, the most suitable process is $t\bar{t}Z$ production. The coefficients C_V and C_A are accessible through the $t\bar{t}Z$ cross section. If their values are modified, the normalisation of the Lagrangian can vary and the experimental yields are influenced. Therefore, a $t\bar{t}Z$ cross section measurement is already sensitive to T_t^3.

Even more detailed information about the coupling is accessible through the Z boson kinematics and spin. When the Z boson is produced, the share of left- and right-handed coupling determines its helicity. All three polarisation states are possible: left-handed, longitudinal and right-handed. The spin information and kinematics of the Z boson are passed on to the decay products and affect their kinematic distributions. The comparison of measurements to theory predictions allows the extraction of the value of T_t^3 provided that the signal kinematics are precisely modelled.

Studies documented in Ref. [40, 41] show the dependence of angular distributions on the coupling factors. The authors investigated the trilepton final state in proton-proton collisions at $\sqrt{s} = 13$ TeV. They found that the opening angle $\Delta\phi_{\ell^+\ell^-}$ of the two charged leptons coming from the Z boson is sensitive to $C_{1,V/A}$. It is even more sensitive to the values $C_{2,V/A}$. The latter parameters can alternatively be determined by analysing the transverse momentum distribution of the Z boson.

In conclusion, the $t\bar{t}Z$ process offers a unique opportunity to determine the third component of the weak top quark isospin. A cross section measurement gives first findings, whereas the examination of angular distributions is more sensitive to T_t^3.

2.4.2. Production Mechanisms

Four Feynman diagrams describe $t\bar{t}Z$ production and one diagram $t\bar{t}W$ production at lowest order as depicted in Figure 2.5. In the top right diagram, the vector boson comes from initial state radiation (ISR) and in the other three (bottom) the Z boson is produced by final-state radiation (FSR). Only in the latter cases, a direct tZ vertex is present revealing the characteristics of the coupling.

Cross section calculations for $\sqrt{s} = 13$ TeV proton collisions have been published using the MadGraph5_aMC@NLO (MG5_aMC) framework [42]. They show that the largest uncertainty on the total cross section originates from choice of the renormalisation and factorisation scale $\mu_0 = \mu_R = \mu_F$. The authors of MG5_aMC use $\mu_0 = \frac{H_T}{2}$, where $H_T = \sum_i^N m_{T,i}$ is the sum of the transverse masses of t, $\bar{t}$ and Z. They obtain [42]

$$\sigma_{pp\to t\bar{t}Z} = 759.8^{+74}_{-85}\ (\text{scale})^{+15}_{-17}(\text{pdf})\ \text{fb}.$$

In another publication [43], the scale is defined as geometric mean of all final-state transverse masses $\mu_0 = (\prod_i^N m_{T,i})^{\frac{1}{N}}$. The cross section value is approximately 15% higher, but agrees within the uncertainties[9]. The influence of electroweak corrections is investigated in Ref. [44] and found to be small compared to scale choice and NLO contribution in QCD.

In contrast to the $t\bar{t}Z$ process, the charged vector boson W can only be emitted by an incoming quark (see top left diagram in Figure 2.5). Thus, neither gluon fusion processes nor FSR play a role. The processes $t\bar{t}W^+$ and $t\bar{t}W^-$ do not have the same cross section, as depicted in Figure 2.6. The reason is that the colliding protons contain two valence up quarks and one valence down quark. Hence, the coalescence of $u\bar{d}$ occurs statistically more often than $\bar{u}d$ and therefore the W^+ boson emerges more frequently. At 14 TeV, the enhancement roughly amounts to a factor of 2 [45]. The 13 TeV cross section for the combined $t\bar{t}W$ process shows similar scale dependencies as the $t\bar{t}Z$ process. It is calculated with the same framework as above

[9] Qualitatively, the different cross sections can be explained with the scale choice. The value of $\frac{H_T}{2}$ is larger than the arithmetic mean of transverse masses $\frac{H_T}{3}$, which in turn is larger or equal to the geometric mean. Hence, in the latter case the strong coupling constant is larger resulting in a higher cross section.

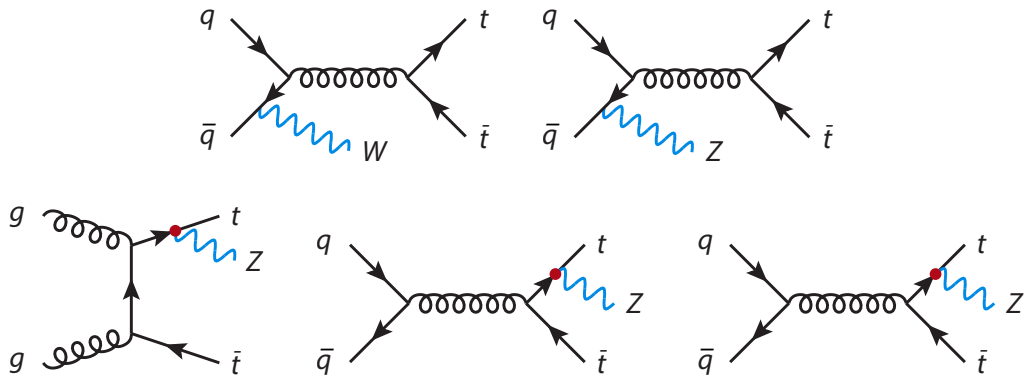

Figure 2.5.: LO production of a $t\bar{t}$ pair accompanied by a W or Z boson. The Z boson can be produced in ISR (top) and FSR (bottom), while only ISR contributes to $t\bar{t}W$ production. The red dot indicates the interaction vertex of top quark and Z boson.

and found to be [42]

$$\sigma_{pp\to t\bar{t}W} = 566.2^{+64}_{-61}(\text{scale})^{+10}_{-8}(\text{pdf})\ \text{fb}.$$

In proton-proton collisions, top quark pairs are mostly produced by gluon fusion, as quoted above. This changes if an additional vector boson is emitted. Only quark-antiquark annihilation is responsible for $t\bar{t}W$ production, because only quarks in the initial state can radiate off a W boson. The production mechanism of $t\bar{t}Z$ is comparable to the bare $t\bar{t}$ case, but quark-antiquark annihilation is enhanced due to the ISR contribution. A Sherpa v2.2 [46] (Sherpa) simulation at LO was performed to assess this enhancement at different centre-of-mass energies. The results indicate that $t\bar{t}Z$ arises to 65% from gluon fusion and to 35% from quark-antiquark annihilation at 13 TeV. Details about the simulation can be found in Appendix A.

2.4.3. Measurements

As the experimental signatures of $t\bar{t}W$ and $t\bar{t}Z$ are very similar and as the cross sections are alike, a combined measurement of both signals is reasonable. At LHC experiments multiple analyses have been conducted. Using data recorded at centre-of-mass energies of $\sqrt{s} = 7$ TeV, the ATLAS collaboration set upper limits to the $t\bar{t}Z$ process [47], while the CMS collaboration measured $t\bar{t}Z$ and $t\bar{t}V$ cross sections corresponding to a $3.3\,\sigma$ and $3.0\,\sigma$ excess over the background-only hypothesis, respectively [48].

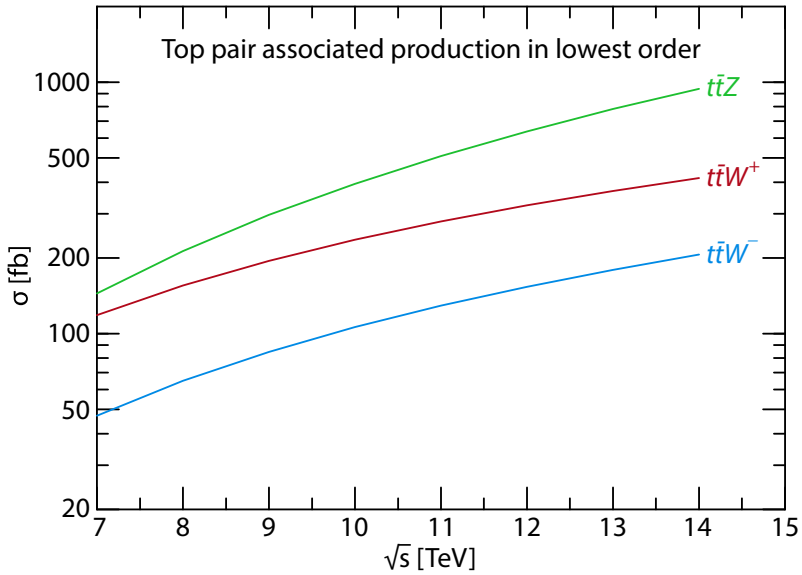

Figure 2.6.: The cross sections for $t\bar{t}V$ processes as a function of the centre-of-mass energy in proton-proton collisions calculated at lowest order [45]. The cross sections increase with the centre-of-mass energy. The positive W^+ boson is produced more frequently than the negative W^-.

The same processes have also been investigated at $\sqrt{s} = 8$ TeV. In their most recent combination, the CMS collaboration reported evidence for the $t\bar{t}W$ and observation of the $t\bar{t}Z$ process [49]. The ATLAS collaboration performed a simultaneous fit of both processes and published the observation of the $t\bar{t}W$ and evidence for the $t\bar{t}Z$ process [50]. All measurements agree with the SM prediction. The exact numbers are listed in Table 2.3.

Both ATLAS and CMS follow a similar approach in their analyses. They divide data into several analysis regions and search for signal events in the dilepton, trilepton, and tetralepton[10] channels. The dilepton region is further divided into an opposite-sign and a same-sign region. The latter one contains two charged leptons with the same charge and is therefore dedicated to selecting $t\bar{t}W$ events. One lepton comes from a semileptonic $t\bar{t}$ decay and the other one from the associated W boson. The region with oppositely charged leptons aims at selecting all-hadronic $t\bar{t}$ decays and Z bosons decaying into charged leptons. If the leptons fall within a mass window of 10 GeV around the Z mass and have the same flavour, the event is accepted. In addition, the ATLAS analysis studies the region outside the Z window in order to also be sensitive to $t\bar{t}W$.

The trilepton final state aims at detecting both $t\bar{t}W$ with a dileptonic and $t\bar{t}Z$ with a semileptonic $t\bar{t}$ decay. Similarly to the dilepton channel, a Z window cut

[10]Lepton in this sense refers to charged, long-lived leptons, i.e. electron and muon.

Signal process	Collaboration	Cross section	Significance
$t\bar{t}W$	ATLAS	369^{+100}_{-91} fb	5.0σ
	CMS	382^{+117}_{-102} fb	4.8σ
$t\bar{t}Z$	ATLAS	176^{+58}_{-52} fb	4.2σ
	CMS	242^{+65}_{-55} fb	6.4σ
$t\bar{t}W + t\bar{t}Z$	ATLAS		7.1σ

Table 2.3.: Overview of LHC measurements for $t\bar{t}$ and associated vector boson production at $\sqrt{s} = 8$ TeV. In each cross section measurement the other process is fixed to its SM value. The last column states the significance with which the background hypothesis is excluded. Background refers to SM processes except the signal process.

is used to separate leptonic Z from leptonic W decays. The final state with three leptons is mainly sensitive to $t\bar{t}Z$.

Finally, the tetralepton channel targets $t\bar{t}Z$ production with a leptonically decaying $t\bar{t}$ system. Again, the invariant mass cut is used for two oppositely charged leptons. After categorising, both ATLAS and CMS use MVAs (neural networks or boosted decision trees) in some regions, to reduce remaining background contamination.

First results at 13 TeV centre-of-mass energy have recently been published using data collected in 2015 [51, 52]. The analysis by ATLAS pursues the previous strategy using final states with two to four leptons, while CMS focuses on $t\bar{t}Z$ in the tri- and tetralepton channel. Both measurements are less significant than former ones at 8 TeV due to the smaller integrated luminosity of the datasets. They are consistent with the SM.

3. Monte Carlo Event Generation

Often, when performing an experiment, not the result itself is enlightening, but rather the comparison to expectations. The a-priori predictions arise from theoretical calculations. In high energy experiments, there are obstacles when it comes to predictions on the level of experimental measurements. These difficulties can be overcome with MC generators.

Nature is probabilistic on quantum mechanical scales. Matrix elements describe the transition probability from one state to another. They can be calculated from first principles using perturbation theory in QCD, but divergencies in phase space integration make computations cumbersome. MC integration allows to perform this phase space integration and accounts for the randomness of quantum mechanics.

When protons are collided at the LHC, the involved energies span a wide range with momentum transfers of TeV down to MeV. Therefore, cross sections depend on different kinematic energy scales and the related coupling constants. MC generators solve this issue with factorisation theorems. They use the fact that interactions at different energies can be computed separately. Thus, high-energetic interactions are established with perturbation theory, whereas the non-perturbative, low-energetic regime is assessed with empirical models. Three fundamentally different stages are implemented in event generators. Their major aspects are outlined in the next sections following the review in Ref. [53].

3.1. Hard Process

The entire event generation is built around the hard scattering process. It simulates basic interactions starting with initial-state partons. The production of heavy particles requires a high momentum transfer between the initial quarks. Thus, small values of the strong coupling constant are involved and QCD processes can be calculated perturbatively. The cross section σ of a process $ab \to n$ can be computed

with

$$\sigma = \sum_{a,b} \int_0^1 \mathrm{d}x_a \mathrm{d}x_b \int \mathrm{d}\Phi_n \, f_a^{h_1}(x_a, \mu_F) f_b^{h_2}(x_b, \mu_F) \cdot \frac{1}{2\hat{s}} |\mathcal{M}_{ab\to n}|^2(\Phi_n; \mu_F, \mu_R).$$

The sum takes into account all initial-state partons a, b in the colliding hadrons h_1, h_2 and the following integral considers their momentum fractions x_i (with $i = a, b$). The PDFs $f_i^h(x_i, \mu_F)$ of both interacting partons are integrated over the phase space Φ together with the squared matrix element $|\mathcal{M}_{ab\to n}|^2$. The factor $\hat{s} = x_1 x_2 s$ accounts for the available centre-of-mass energy. MC methods are used to perform the phase space integration and to sum over helicity and colour combinations.

The PDFs $f_i^h(x_i, \mu_F)$ depend on x_i and the factorisation scale μ_F. This scale separates high-energetic interactions ($\mu > \mu_F$) from low-energetic interactions ($\mu < \mu_F$). The former ones are calculated perturbatively, while the latter ones are included in the PDF. The QCD calculation does not depend on the selected value of μ_F, if all computation terms are considered. For approximations within perturbative calculations, the precise value of μ_F is important. It is typical to set $\mu_F = \mu_R = Q^2$. Usually, values for the hard scale Q^2 are chosen to be in the order of the produced particle masses.

In addition to LO diagrams, loop and radiation corrections at higher orders contribute to the inelastic scattering. These diagrams are of NLO or even higher order in α_s and their evaluation increases the precision of predictions. While the additional terms can have large impact on the cross section, they have less influence on the event topology. To minimise the computation time, events are simulated at lower orders (typically NLO) and subsequently their yield is scaled to the most precise cross section prediction available using so-called K-factors $k = \frac{\sigma^{\text{best theor. prediction}}}{\sigma^{\text{in MC sample}}}$. An often used compromise between high precision and simulation effort is the tree-level generation of higher-order matrix elements. This way, real emissions are simulated, but virtual corrections and interference terms are neglected. This is in particular helpful for a better description of jet multiplicities.

3.2. Parton Shower

After the hard process is generated, strongly interacting particles radiate a vast number of secondary partons. These colour-charged particles can emit even more partons producing a parton shower. At low energies, the partons eventually hadronise. This hadronisation is not perturbatively accessible due to large values of α_s and needs

to be modelled. Radiative processes in the energetic range between Q and $\mathcal{O}(1\text{ GeV})$, however, can be derived from first principles. Parton shower implementations use algorithms derived from QCD to simulate these strong interactions.

A hard process is considered generating the partons i with a cross section σ_0. Then, the differential cross section for the same process with an additional parton j branched off by the partons i with momentum fraction z and opening angle θ is given by

$$\mathrm{d}\sigma \;\approx\; \sigma_0 \sum_i \frac{\alpha_s}{2\pi} \frac{\mathrm{d}\theta^2}{\theta^2}\, \mathrm{d}z\; P_{ji}(z,\phi)\, \mathrm{d}\phi. \tag{3.1}$$

This expression is collinearly divergent when the radiation angle θ approaches $\theta \to 0$. $P_{ij}(z,\phi)$ are coefficients depending on the spin orientation ϕ. They diverge when the energy z of the splitting parton converges to $z \to 0$, a soft divergence.

Although these infinities imply that the probability of a splitting associated with equation (3.1) grows infinitely high, there are no direct consequences. Physical observables cannot distinguish between one parton and two collinear ones, provided both systems have the same momentum. As this is the case in both the collinear and infrared limit, both divergences have no physical meaning and a cut-off for low transverse momenta can be implemented in parton shower algorithms. The cut value defines the energy-dependent probability of a parton not to branch, in which case it keeps its kinematic properties. If, conversely, a parton splits up, it is created far enough from the collinear and infrared divergencies. The same algorithm is applied again for its children, such that they can in turn radiate partons. Hence, the iterative procedure creates a parton shower down to energies where perturbative approximations become imprecise and hadronisation models are applied. This showering is not only applied for the final-state particles (forward shower), but also for the initial-state (backward shower) starting at the hard interaction propagating back to the colliding particles.

As illustrated in section 3.1, higher-order corrections can create additional partons on matrix element level. The parton shower produces the same results. Matrix element calculations are suited for perturbative QCD. They describe angular distributions in different spatial directions and hard emissions very well. In contrast, parton showers use approximations in the soft regime. They describe soft and collinear emitted partons accurately and simultaneously take care that divergences are avoided. Thus, combining the approaches exploits the advantages of both.

It is important to note that this introduces additional difficulties, namely event overlap. A process generated at NLO on matrix-element level comprises diagrams with emission of real partons. The same final state can also be achieved with the

LO diagram where partons are created by the parton shower. The same applies for multiple tree-level matrix elements of different order followed by parton showers. Therefore, sophisticated matching and merging schemes are used to inhibit double-counting and under-counting. Various mechanisms are implemented in different MC generators. The MG5_aMC generator, for instance, uses event-based cuts for shower merging. An event is rejected if partons produced on matrix element level are below a certain cut-off scale or if partons produced during the parton shower are above this cut-off scale. In other words, events are removed, if the same final state can be produced with another, non-vetoed production mechanism.

3.3. Hadronisation

The parton shower simulates the propagation of quarks and gluons as long as shower approximations hold true. After that, the growing strong coupling constant renders perturbation theory ineffective. Instead, hadronisation models describe further interactions of partons in two steps. First, associated partons are produced, which is called "fragmentation". Subsequently, all these coloured partons are combined into colourless hadrons. Two main hadronisation approaches are the string and cluster model, whose methodologies and prediction powers are very complementary.

The string model was developed along with Pythia [54, 55] and is based on the hypothesis that quarks are linearly confined on large scales. This assumption is supported by hadron spectroscopy and lattice QCD calculations predicting a string constant of $\kappa \approx 1 \frac{\text{GeV}}{\text{fm}}$. This value can be understood as the energy per unit length stored in a string between two quarks. The basic idea of fragmentation is illustrated best for two quarks q and $\bar{q}$ which originate from the same location and are connected by a string (see Figure 3.1(a)). As they move apart, the string energy increases. At some point the string breaks and releases its energy producing a new $q'\bar{q}'$ pair. This novel pair splits up such that the quarks are grouped $q\bar{q}'$ and $q'\bar{q}$. If the invariant mass of one of these systems is large enough, they do again separate in the same way as before. This iterative process stops, once all the available energy is consumed.

The string model implements the fact that, classically, a quark pair carrying mass or transverse momentum cannot be produced at the same point by introducing the tunnelling effect. The quarks are quantum-mechanically created at one point and can only escape, if they overcome a barrier. The tunnelling probability vanishes for high quark masses and thus the occurrence of heavy quarks is suppressed with $u : d : s : c = 1 : 1 : 0.3 : 10^{-11}$. So far, the model only generates mesons and there are multiple ways to include baryon production. The easiest is to create a diquark

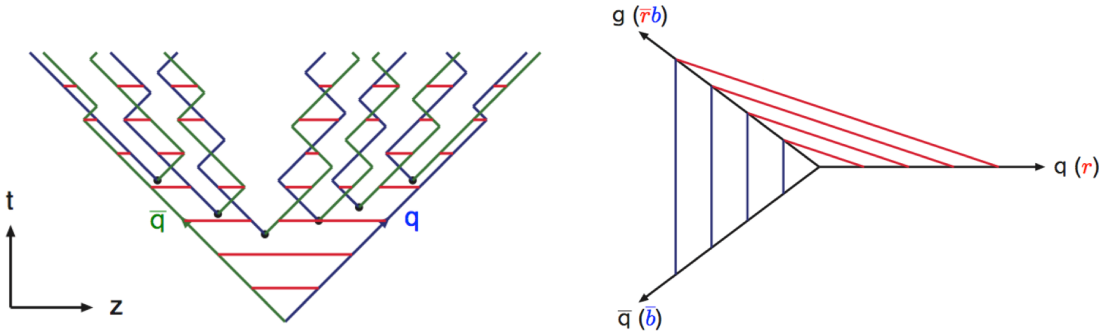

(a) (b)

Figure 3.1.: Fragmentation in the string model. (a) In the fashion of a Minkowski diagram, the particle movement in time is depicted in the upward direction. Quarks are depicted in blue, antiquarks in green. As high energetic quarks move apart, a red string develops between them. When enough energy is stored in the string, a new quark pair is produced. Bound $q\bar{q}'$ pairs are sketched as oscillating around each other. (b) The propagation of a $q\bar{q}$ pair and an additional gluon is depicted as movement in the outwards direction. Strings only develop between quarks and the gluon. They break in the same scheme as in (a).

pair, when a string breaks. This diquark pair can then form a baryon together with a single quark from elsewhere.

A particularly powerful feature of the string implementation is that it can easily be extended to gluons. Figure 3.1(b) shows the configuration of two quarks and a gluon moving apart. In this case, the quarks do not form strings between each other, but only to the gluon. A gluon can therefore be understood as a kink in a string. Like before, quark-antiquark pairs are produced by breaking strings and the propagation rules for $q\bar{q}$ pairs apply again. As a consequence, most quarks are produced in the region between quarks and gluons, while the quark-antiquark region is depleted. This is in agreement with experimental observations.

Another widely used hadronisation procedure is the cluster model. It is for example utilised in SHERPA. Its underlying idea is to combine all generated partons to colourless clusters such that partons close in phase space are combined. Each of these clusters decays independently into hadrons.

The cluster model is based on the preconfinement property of parton showers. A hard interaction is considered at the scale Q and a subsequent parton shower. Showering is aborted at an energy scale $Q_0 \ll Q$ and the partons form clusters. According to preconfinement, the mass distribution of these clusters does not depend on Q. This property is suitable to model the transition from parton shower to hadronisation.

When the parton shower discontinues at Q_0, many quarks and gluons are present. In order to combine them into clusters, the cluster model first forces all gluons to split up into quark or diquark pairs, $q\bar{q}$ or $d\bar{d}$. Although this is a rather abrupt and unphysical splitting, it can be motivated by the values of α_s at very low energies. The strong coupling constant is found not to increase beyond all measure, but has a finite effective value. This is realised in the cluster model with the artificially increased quark and decreased gluon abundance. It enhances colour screening and accounts for the low-energetic behaviour of α_s. Furthermore, the $g \to q\bar{q}$ splitting can also explain high abundances of soft photons in $Z \to q\bar{q}$ events. The excessive photons cannot come from gluons, but can be radiated by the additional quarks.

To summarise, at the scale Q_0 gluons are split into quarks and subsequently nearby quarks form clusters which follow a universal invariant mass distribution. In the next step, all clusters must be decayed, which can be modelled in various ways. A rather plain method is to pick any two-body decay according to the respective likelihood of occurrence. This probability depends on flavour composition, spin configuration, kinematics and phase space. This way of modelling agrees with the observation that final jet signatures are mainly determined by cluster kinematics and only subordinately by cluster decays. Furthermore, kinematic considerations intrinsically disallow heavy flavours and suppress strangeness. Moreover, the difference between gluon and quark jets is automatically simulated. Gluon jets are supposed to have higher hadron multiplicities that show softer spectra with a wider dispersion. This behaviour is emulated, as gluon jets are generated from two quarks in close spatial directions.

In the described implementation, only a few free parameters are needed and the most critical one is the cut-off scale Q_0. Recent realisations, however, are more advanced and use more parameters. They correct for heavy particle yields, kinematic distributions and balance meson and baryon production. In addition, they treat clusters with high masses in a different way.

4. The Experiment

4.1. LHC

The world's largest particle collider is presently the LHC [56]. It is located at the "Organisation européenne pour la recherche nucléaire" (CERN) laboratory close to Geneva, Switzerland. Particles are accelerated in a circular tunnel with 26.7 km circumference. Two beam pipes run along the tunnel and are filled with bunches of protons or lead ions. The protons come from a multi-stage acceleration system and are injected into the LHC at energies of 450 GeV. They traverse both beam pipes in opposite directions. To achieve the peak luminosity, every single bunch contains $1.15 \cdot 10^{11}$ protons and moves almost with the speed of light. Ordinarily, two consecutive bunches are 25 ns apart corresponding to about 7.5 m spacing. This way a designed peak luminosity of $\mathcal{L} = 10^{34} \frac{1}{\mathrm{cm}^2\mathrm{s}}$ can be accomplished. So far, the ATLAS experiment has reported a peak luminosity of $\mathcal{L} = 5.0 \cdot 10^{33} \frac{1}{\mathrm{cm}^2\mathrm{s}}$ in Run 2. An integrated luminosity of 3.9 fb^{-1} was recorded in 2015 at 13 TeV.

Once the protons are inside the LHC ring, electromagnetic cavities further accelerate them and a sophisticated setup of magnets deflects and collimates the particle beam, which would disperse otherwise. When the beam particles reach an energy of 6.5 TeV, they are collided at four interaction points along the LHC tunnel. Around every collision point, sophisticated detectors are built to measure the collision remnants to reconstruct the particle interactions.

The ALICE experiment is the only LHC experiment specialised in ion collisions. In these collisions, the energy density is so high that a state with unbound quarks and gluons is created, the so-called "quark-gluon-plasma". Analysing the decay products of this high-energetic matter, which resembles the state of our early universe, is the purpose of the ALICE detector. The LHCb experiment uses proton-proton collisions to investigate the origin of CP violation. To this end, the role of b quarks and the decay of the $b\bar{b}$ meson in particular is examined. The ATLAS and CMS experiments are optimised to detect all kinds of decay particles from proton-proton collisions. Tracking and analysing particles allows to reconstruct the intrinsic particle interaction. Thus, sophisticated analyses can infer properties about intermediate particles such as the Higgs boson discovered during Run 1. While the ATLAS

experiment sets the focus on toroidal magnets and accurate muon chambers, the CMS approach is to have a compact setup with a strong solenoidal magnetic field and exclusively silicon as tracking detector material. Pursuing the same purposes, both experiments are built complementary and are supposed to deliver independent results.

The general detector design is driven by the harsh conditions predetermined by the LHC. The high luminosity and the short time between collisions demand fast data readout and efficient data reduction. Due to the extensive occupancy, the inner parts of the detectors in particular need to withstand a high radiation dose. The following section gives a short overview of how the ATLAS experiment provides high-resolution particle tracking and energy measurements on a large solid angle.

4.2. ATLAS experiment

The ATLAS experiment [57, 58] is a cylindrical setup of various detectors as depicted in Figure 4.1. All detectors cover almost the full azimuthal angle ϕ around the beam axis z and a large part of the polar angle θ from the beam axis. The polar angle is usually referred to as pseudorapidity[1] $\eta = -\ln\tan\frac{\theta}{2}$.

Closest to the interaction point the Inner Detector is responsible for tracking. Its three subdetectors, the Pixel Detector, Semiconductor Tracker (SCT) and Transition Radiation Tracker (TRT), follow different approaches to unite radiation hardness and high granularity for vertex reconstruction. The Pixel Detector comprises four barrel layers around the beam axis and end-cap detectors perpendicular to the beam. It detects traversing particles in silicon pixels, as they leave a trace of electron-hole pairs. The pixels are finely segmented in ϕ and coarser in z. This way high azimuthal resolution and precise determination of transverse momentum imbalance are accomplished.

The SCT surrounds the Pixel Detector and consists of barrel and end-cap layers as well. The silicon sensors have microstrip electrodes, whose alignments differ by a small angle. Thus, it provides two-dimensional, binary hit information. In order to minimise radiation damage accompanied by signal drop after some operation time, both the Pixel Detector and the SCT are operated below $-5°$ C.

The Inner Detector's outermost part is the TRT. It uses straw tubes filled with a $Xe/CO_2/O_2$ mixture to detect ionising particles. The tubes are arranged in z direction for barrel layers and in radial direction for end caps. In addition, they

[1] Pseudorapidity equals the rapidity of a particle $y = \frac{1}{2}\ln\left(\frac{E+p_L}{E-p_L}\right)$ in the massless limit. p_L refers to the longitudinal particle momentum. The rapidity is a handy quantity, because differences in rapidity $\Delta\eta$ are Lorentz invariant.

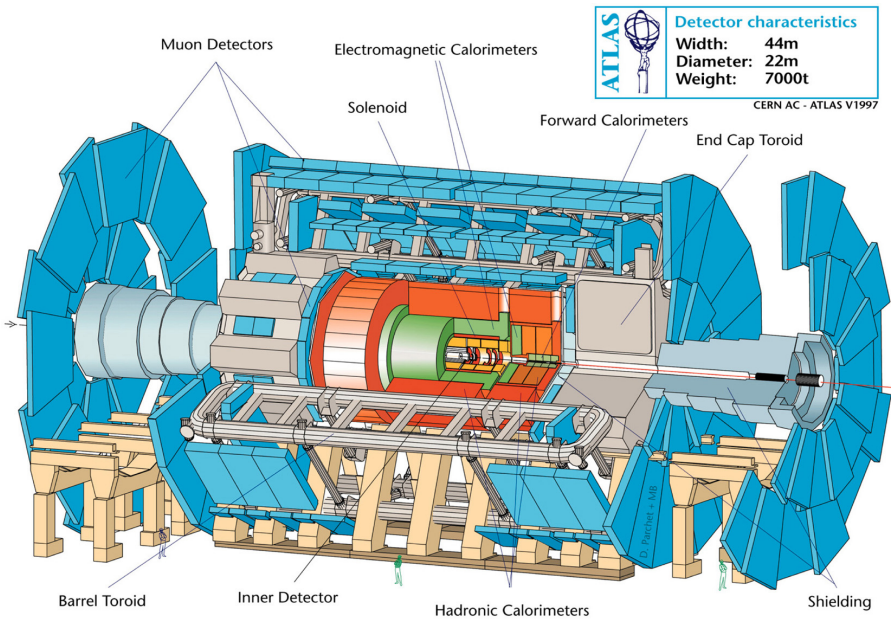

Figure 4.1.: The ATLAS detector.

are covered with a transition radiation material. Charged particles traversing the foil create radiation that leaves an additional signal in the detector. This helps to identify electrons produced in the collision. The TRT covers a pseudorapidity region of $|\eta| < 2.0$, while the Inner Detector and SCT cover $|\eta| < 2.5$.

Multiple hits in all detector layers ensure a reliable primary and secondary vertex reconstruction and electron identification in $|\eta| < 2.5$ and $|\eta| < 2.0$, respectively. The entire Inner Detector is penetrated by a 2 T magnetic field in z direction in order to deflect charged particles. This allows to determine the particle momentum.

The calorimeters are designed to absorb all kinds of particles and to determine their energy. The electromagnetic calorimeter is located just outside of the Inner Detector. Its innermost part is a presampler detector ($|\eta| < 1.8$) measuring the energy that the particle has already lost before entering the electromagnetic calorimeter. The main part of the electromagnetic calorimeter is a sampling detector. It uses lead to decelerate and to shower incoming particles and liquid argon to measure the signal and to quantify the amount of shower particles. It consists of 3 (2) active layers in the region $|\eta| < 2.5$ ($2.5 < |\eta| < 3.2$). The innermost layer is finely segmented in η in order to precisely determine the particle position. The main signal is deposited in the second layer and the third layer usually detects the shower tail. The quantity "radiation length" X_0 states after which distance the energy of the penetrating particle decreases to $\frac{1}{e}$ on average. The electromagnetic calorimeter has a radiation

length of $22\,X_0$ in the central part increasing to $36\,X_0$ in the higher rapidity area. A forward calorimeter covers the region close to the beamline $3.1 < |\eta| < 4.9$.

While most of the electrons and photons leave all their energy in the electromagnetic calorimeter, the hadrons traverse it without losing much energy. They are detected in the hadronic calorimeter, which consists of three barrels arranged side-by-side, two end-cap wheels and a forward calorimeter. The barrels use steel as moderator and scintillator tiles to measure the signal, while the end-cap calorimeter uses interlaced copper and liquid argon. Copper is used in the first layer in order to be more sensitive to electromagnetic showers and tungsten is used in the following two layers.

Apart from neutrinos, muons are the only particles that regularly travel through all the detector parts rather unimpeded. To provide an additional measurement of their momentum, the muon spectrometer works together with the toroid magnets. They supply a spatially varying magnetic field approximately perpendicular to the muon trajectory in all relevant rapidity regions. The particle deflection is measured by three barrel layers and three end-cap layers. In the central region, gas-filled monitored drift tube chambers detect the muon track and in the forward region multiwire proportional chambers are used. Additional detectors are dedicated to give a fast response for triggering purposes.

Since not all the data recorded by the ATLAS experiment can be stored, efficient triggering and event selection is necessary. On the first level, the trigger system searches for various basic signatures, for example high transverse momentum of electrons or muons, large deposits in the calorimeter and hadronic τ decays. On a second level, the regions, which discovered the signature on level 1, are further examined. If the event matches all criteria, a high-level trigger uses full granularity data of most detector parts to select events for permanent storage. This way, after four seconds of processing, the event rate is reduced by a factor of $4 \cdot 10^4$ to approximately 1 kHz [59].

5. Validation of Monte Carlo Simulations

Chapter 3 gave a brief overview of event generation in MC simulations. It illustrated that these simulations are by no means straightforward, but instead contain different models, various approximations and several parameters. There are countless ways to implement various phenomena. In Run 1, MC generators were used for numerous analyses and their overall performance was good. In the transition to Run 2, however, the generators have undergone several changes to further improve the precision of calculations.

In general, research is tending towards higher-order calculations of matrix elements and showering. On matrix element level, the two approaches of multi-jet merging and NLO precision in QCD calculations enhance the accuracy. In parton showers, NNLO computations are becoming available and improve theoretical predictions. In addition, more specific changes have to be considered. The centre-of-mass energy has almost doubled. In this context, also a new PDF became available, namely `NNPDF`. In contrast to the former `CTEQ` family, it includes more recent fits at higher energies promising a more exact description of data. The generation framework on the ATLAS side is also constantly being developed. Multiple updates of technical and physical aspects require that their implementation be validated.

It is essential to ensure that simulations describe theory expectations, before they are compared to data. Deficient simulations could significantly deviate from experimental data and could lead to wrong conclusions about underlying physics. To avoid this scenario, the ATLAS collaboration has a standard validation procedure for MC generators. The different steps of this validation policy are introduced in section 5.1. Afterwards, section 5.2 shows detailed studies of $t\bar{t}Z$ processes. Some of this work was documented in an ATLAS public note [60] dedicated to the validation of $t\bar{t}V$ and $t\bar{t}H$ simulations. The first analysis using these datasets was also published recently [51] in the context of first $t\bar{t}V$ cross section measurements at 13 TeV.

5.1. Validation procedure in ATLAS

For new versions of MC simulations, validation studies [61] need to be performed. The thoroughness and the kind of scrutiny depend on the changes with respect to previous versions. An entirely new MC generator or setup, for example, is compared to existing data, based on a published measurement. Object definitions and cuts from the analysis are applied to newly generated samples. Then, the resulting distributions are compared to data and other established generator setups. Based on the ability to reproduce data, the novel generator setup is rejected or found suitable.

Minor upgrades to successive generator versions happen regularly, as well as modifications in a specific generator component, eg. a different tune or another parton shower modelling. In this case, the two consecutive generator setups are compared to another. A "reference" and a "monitored" sample are generated with the "old" and "new" framework. They are compared in a rather automated procedure and their agreement is estimated with statistical methods in plenty distributions. Sanity checks are also performed and technical details as naming conventions, log files and cross sections are verified. If no unexpected discrepancy arises, the new generator setup is accepted.

Before a sample is used for physics analyses, additional studies related to the specific process are performed. Several MC generators are compared and checked for consistency by comparing various kinematic distributions. The focus lies especially on generator independent observables. Systematic uncertainties are also estimated in this step. To this end, additional samples are generated with varied parameters to estimate the influence of the scale choice, for example.

5.2. Validation studies of $t\bar{t}Z$ processes

The aim of these studies is to generate reliable and precise $t\bar{t}Z$ datasets for usage in physics analyses. On the way to eventually validating datasets, different samples and configurations need to be tested and compared. The comparisons range from only one changed parameter to entirely different generators and production campaigns. The datasets are analysed in order to improve their modelling and to certify that no errors are introduced in different steps. When the samples are found to be plausible, they are validated.

MG5_aMC and Sherpa provide NLO calculations and multileg merging for the $t\bar{t}Z$ process. All following studies are based on these matrix element generators. Separate simulations are performed for Z decays into charged leptons. These leptonic decays ($\sim$10%) consider a Z/γ^* contribution, whereas decays to neutrinos ($\sim$21%) and quarks ($\sim$69%) are simulated without this interference. Detector effects and

Generator	Order	Process	Cross section [fb] original	NLO
MG5_aMC+Py8	LO	$t\bar{t}Z \to \nu\bar{\nu}, q\bar{q} + 0, 1, 2j$	512.8	683.1
Sherpa	LO	$t\bar{t}Z \to \nu\bar{\nu}, q\bar{q} + 0, 1, 2j$	688.1	683.1
MG5_aMC+Py8	NLO	$t\bar{t}Z \to \nu\bar{\nu}, q\bar{q}$	538.4	683.1
MG5_aMC+Py8	LO	$t\bar{t}\ell^+\ell^- + 0, 1j$	81.7	110.7
Sherpa	LO	$t\bar{t}\ell^+\ell^- + 0, 1j$	113.1	110.7
MG5_aMC+Py8	NLO	$t\bar{t}\ell^+\ell^-$	110.7	110.7

Table 5.1.: Overview of MC samples for $t\bar{t}Z$ processes at $\sqrt{s} = 13$ TeV with their cross sections as obtained by the simulations. The decay of the Z boson is denoted by "$\to$". The simulations with $Z \to \nu\bar{\nu}, q\bar{q}$ are normalised to the NLO cross section from Ref. [42]. Decays to charged leptons are generated separately and include the Z/γ interference. Their cross section is taken from the MG5_aMC+Py8 NLO computation. In LO calculations, additional partons are generated on matrix element level and merged. NLO calculations are inclusive.

reconstruction are not taken into account, since they do not depend on the hard interaction for the most part.

Three production setups are optimised and summarised in Table 5.1. As baseline MG5_aMC LO generates the hard matrix element and is interfaced with Pythia8 v.8.210 (Py8) for parton showering and hadronisation. The dataset is composed of three multileg-merging subsamples with exactly 0 (Np0), exactly 1 (Np1) and 2 or more (Np2) partons. The $Z \to \ell^+\ell^-$ decay only comprises an exclusive Np0 and inclusive Np1 subsample. Matrix element and parton shower are merged with the CKKW-L [62, 63] algorithm using a merging scale cut of $k_T = 30$ GeV. As renormalisation and factorisation scales, $\mu_R = \mu_F = \frac{H_T}{2}$ is chosen. Parton distributions for hard scattering and parton showering are described with the NNPDF2.3LO [64] PDF. For parton showering the A14 [65] tune is used and all final-state particles are directly decayed with Pythia8. As a consequence, their polarisation information is lost at the interface.

Similar to the setup above, another LO dataset is generated with Sherpa. Multileg samples are merged with the ME+PS@LO [66] prescription. A parton shower tune developed by the Sherpa authors and the NNPDF3.0NNLO PDF are used. As the entire event is simulated within Sherpa, the polarisations and spin correlations are conserved. The sample is split up and the scales are chosen similarly to the MG5_aMC LO simulation.

In the last setup MG5_aMC+Py8 is employed again, but this time at NLO. It has the advantage of considering virtual corrections, but might suffer from inferior

jet description. Again, as renormalisation and factorisation scale $\mu_R = \mu_F = \frac{H_T}{2}$ is chosen. The `NNPDF2.3LO` PDF is used in combination with the `A14` tune for PYTHIA8. In contrast to the LO setup, top quarks and vector bosons are decayed with MADSPIN [67] preserving their spin information.

Final-state hadrons are clustered to jets with the anti-k_T algorithm [68] using a radius parameter of $R = 0.4$. More technical information about all datasets is summarised in Appendix B. Section 5.2.1 reviews 8 TeV simulations to estimate the impact of the changes towards Run 2. Afterwards, a defective simulation and its revised version are discussed in section 5.2.2, before the validated versions of the three mentioned samples are presented.

5.2.1. Validation of New Setup at 8 TeV

In simulations for hadron colliders, PDFs describe both the colliding hadrons and the decays in parton showers. They quantify the amount of valence quarks, sea quarks and gluons in a bound state with their respective momentum fraction. The PDF parametrisation can have large influence on production mechanisms, distribution shapes and also the cross section. In particular, transverse momenta and pseudorapidities are susceptible to PDF modelling.

Two simulations with the baseline setup are compared here. Only events with on-shell Z bosons decaying into charged leptons are considered. The single difference between both samples is the PDF choice. One dataset is generated with the `NNPDF2.3LO` set, the other one with `CTEQ6L1` [69]. While the latter PDF was fitted in 2002 using data from various experiments, the `NNPDF2.3LO` set was obtained in 2012 including more recent LHC data. Therefore, the novel PDF is expected to yield higher precision and was chosen as ATLAS baseline for Run 2.

Table 5.2 shows that the total cross section of both processes differs by a factor of $\frac{\sigma_{\text{CTEQ}}}{\sigma_{\text{NNPDF}}} \approx 0.7$, while smaller differences were expected. This discrepancy was identified as bug in the job setup. To account for this, the following distributions are normalised. The issue was fixed for subsequent MC productions.

PDF	Process	Cross section [fb]
`CTEQ6L1`	$t\bar{t}Z \to \ell^+\ell^- + 0,1j$	9.2
`NNPDF2.3LO`	$t\bar{t}Z \to \ell^+\ell^- + 0,1j$	13.2

Table 5.2.: Overview of the datasets used for PDF comparison. The $t\bar{t}Z$ process with $Z \to \ell^+\ell^-$ is generated with the baseline setup at LO. Only the on-shell Z contribution is taken into account. The cross section values are affected by a faulty setup.

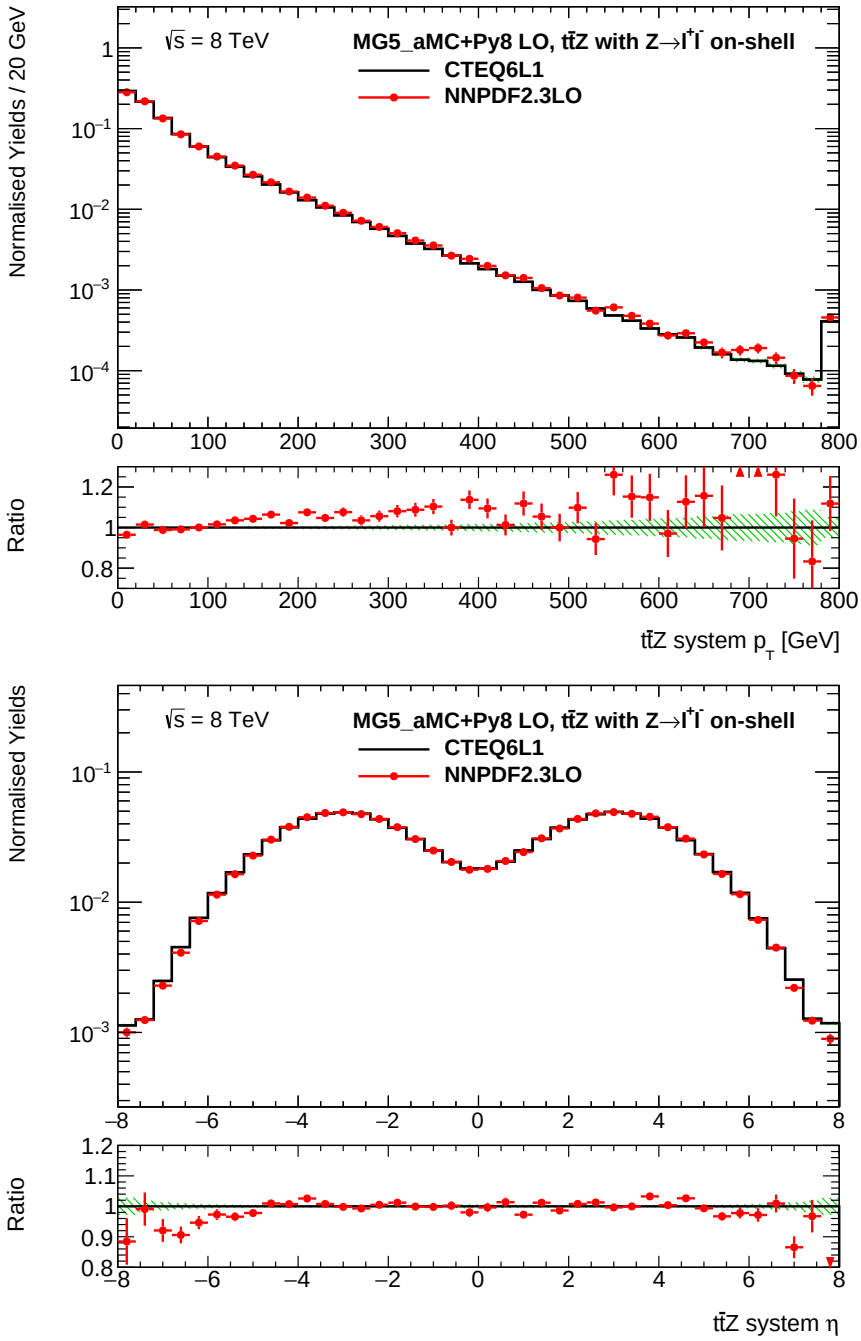

Figure 5.1.: The new PDF `NNPDF2.3LO` is compared to the Run 1 choice `CTEQ6L1`. $t\bar{t}Z$ events with an on-shell Z boson decaying into two charged leptons are shown. Both datasets are normalised to unity in order to compare the shapes. Errorbars represent statistical errors in the MC samples.
On parton level, the $t\bar{t}Z$ system shows no significant differences in the η distribution, but deviates in transverse momentum. Harder $t\bar{t}Z$ p_T's are modelled by `NNPDF2.3LO`.

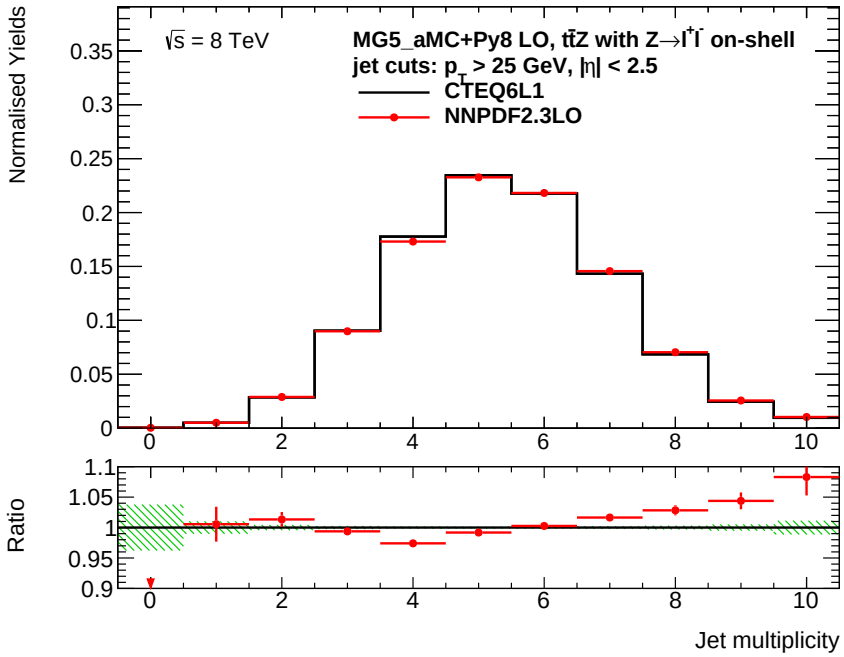

Figure 5.2.: The same simulation is shown as in Figure 5.1. On particle level, the `NNPDF2.3` PDF set produces more jets.

As PDFs are intrinsically connected with matrix element generation, they have large influence on the $t\bar{t}Z$ system. Its transverse momentum and pseudorapidity are depicted in Figure 5.1. A close look reveals that the `NNPDF2.3LO` PDF favours higher transverse momenta and predicts fewer events in the region below 100 GeV. At higher transverse momenta, the systematic difference amounts to approximately 10%. The $t\bar{t}Z$ pseudorapidity distributions are similar for both PDF sets. They only show a modest discrepancy at high $|\eta|$ values, where the new `NNPDF2.3LO` set produces slightly fewer events.

Additionally to hard scattering, PDFs are also involved in modelling soft radiations within the parton shower. Thus, the jet multiplicity in Figure 5.2 is sensitive to the PDF choice. Precise jet modelling is most important in the detector regions covered by the calorimeter above a reconstruction threshold. Hence, only jets with pseudorapidities $|\eta| < 2.5$ and transverse momenta $p_T > 25$ GeV are considered. On parton level, events are expected to comprise 2, 4 or 6 jets in the dileptonic, ℓ+jets and all-hadronic $t\bar{t}$ decay, respectively. The multiplicities 4 and 6 are preferred due to the high branching ratio. On particle level, these distinct values are smeared because of phase space cuts and contingent additional radiation. Therefore, events with 5 jets occur most often. There is a small systematic deviation between the two

samples. Events generated with NNPDF2.3LO are shifted to higher jet multiplicities. This is visible for 4 jets or more.

Also other distributions have been investigated. They are consistent with the remarks outlined above and none of them show large deviations. The PDF CTEQ6L1 and the newer NNPDF2.3LO set produce similar results for $\sqrt{s} = 8$ TeV simulations with small systematic differences. This is a first indication that the new setup can also describe $t\bar{t}Z$ production at 13 TeV consistently.

5.2.2. Validation of 13 TeV Samples

The first $t\bar{t}Z$ simulations generated with the baseline setup at $\sqrt{s} = 13$ TeV show unexpected behaviour, which becomes most apparent in the branching ratios. In the sample with $Z \to \nu\bar{\nu}, q\bar{q}$, too few quarks relative to neutrinos are produced. This is caused by a misconfiguration of the CKKW-L merging. This merging procedure is supposed to reject low-energetic partonic radiation on matrix element level, since this soft phase space region is modelled by the parton shower. The algorithm needs to correctly identify the core process and may only remove particles that can be created in the parton shower. In the defective setup, the phase space cut was also applied to quarks emerging from Z boson decays. As they cannot be produced in the parton shower, they must not be deleted.

This bug was fixed and the simulations were redone with an updated version of MG5_aMC (v.2.3.2, as opposed to v.2.2.3). Table 5.3 contains more details about the samples. The issue is made apparent in Figure 5.3. The branching ratios of the Z boson are depicted for the old and new simulation. Additionally, the values as expected from the SM are shown. They agree well with the revised version.

A more detailed understanding of the CKKW-L algorithm helps to interpret the kinematics related to the mismodelling. After all partons from the hard matrix element are showered, the merging algorithm inspects the strong splittings inside jets. It checks whether daughter particles have transverse momenta below $k_T = 30$ GeV

Generator	Process	Cross sections [fb]	
		$Z \to \nu\bar{\nu}$	$Z \to q\bar{q}$
MG5_aMC(2.2.3)+Py8, "old"	$t\bar{t}Z \to \nu\bar{\nu}, q\bar{q} + 0j$	39.24	83.04
MG5_aMC(2.3.2)+Py8, "new"	$t\bar{t}Z \to \nu\bar{\nu}, q\bar{q} + 0j$	39.42	133.93

Table 5.3.: Two $t\bar{t}Z \to \nu\bar{\nu}, q\bar{q}$ samples with the baseline setup are compared. The updated simulation includes correct CKKW-L merging. Only datasets without additional partons are compared. Although these are not physically meaningful, the different modelling is equally well apparent in the Np0 subset.

with respect to their mother particles. Only in this case, the jet is kept. Conversely, partons radiated off during matrix element generation are vetoed if they have transverse momenta below $k_T = 30$ GeV.

In case of the corrupted sample, this last step is also applied for quarks originating from Z boson decays. Thus, decays with little transverse momentum are rejected. This affects quarks produced rather parallel and antiparallel to the Z boson direction of flight. As a consequence, a clean cut of 30 GeV on the quark transverse momentum in the Z boson rest frame is expected. Ramifications of this are visible in the quark p_T in the detector frame. Figure 5.4 shows that this distribution is continuous down to 30 GeV, where the distorted simulation drops steeply and the correct one continues smoothly. The sharp edge corresponding to the cut value k_T is smeared, because Z bosons carry non-zero transverse momenta.

Figures 5.5 and 5.6 illustrate how remodelling affects other kinematic variables. The occurrence of low p_T quarks is visible in pseudorapidity distributions. If transverse momenta are small, the z component contributes more to the total momentum. Hence, the $|\eta|$ distribution is shifted to higher values in the new sample.

In Figure 5.6, the opening angle of the $q\bar{q}$ pair from the Z boson is parametrised with $\Delta R = \sqrt{\Delta\phi^2 + \Delta\eta^2}$. Larger opening angles are seen with higher amounts in the repaired simulation, because more quarks are emitted parallel and antiparallel to the Z boson direction of flight. As Z boson transverse momenta are small in most events, this corresponds to larger $\Delta R(j, j)$ values. The transverse momentum of the $t\bar{t}$ system has smaller values in the updated sample. This originates from the fact that more events with lower Z p_T exist. Less recoil is introduced against the $t\bar{t}$ system and results in a shifted p_T distribution.

These comparisons show that small irregularities can compromise all modelling efforts. The deficiency was corrected so that the updated simulation yields more accurate modelling.

So far, only the baseline simulation was presented. In the following, this setup is tested against Sherpa and MG5_aMC+Py8 at NLO as outlined in Table 5.1. This comparison is crucial in revealing modelling disagreement and systematic uncertainties. On truth level, hadronic Z boson decays are selected and the $t\bar{t}$ pair is required to decay in the ℓ+jets channel. This simplifies the interpretation of distributions. Jets are chosen with $p_T < 25$ GeV and $|\eta| < 2.5$.

Basic kinematic variables on parton level are depicted in Figure 5.7. Transverse momenta of the $t\bar{t}$ system from the LO and NLO MG5_aMC+Py8 framework coincide up to 300 GeV, apart from a small discrepancy at low values. Above 300 GeV the LO simulation systematically produces more $t\bar{t}$ pairs. Events generated with Sherpa agree well with MG5_aMC+Py8 NLO, but are slightly more abundant in low and high p_T. The transverse momenta of the Z and $t\bar{t}$ system are

correlated due to conservation of momenta. Consequently, the Z boson p_T yields a similar picture. MG5_aMC+Py8 NLO and Sherpa are comparable, although the latter generator predicts a softer spectrum for transverse momenta. The two MG5_aMC+Py8 distributions are similar up to 300 GeV. Finite sample statistics in the high-momentum tail of the LO sample make a comparison infeasible. Despite the deviations in $t\bar{t}$ p_T, the angular distribution η is in good agreement.

The $t\bar{t}$ system decays in the ℓ+jets channel and the Z boson decays hadronically. Thus, events are expected to yield six partons on matrix element level, which evolve into jets in the parton shower and hadronisation process. Therefore, events with six jets occur most often, as depicted in Figure 5.8. Jets can be missed, because they do not match cuts or because they are emitted close to another jet. Conversely, additional jets can be produced on matrix element level or during the parton shower. These counteracting mechanisms smear the jet multiplicity. In the 6-jet bin, the MG5_aMC+Py8 LO and NLO predictions coincide, while the NLO distribution is shifted to higher values elsewhere. Compared to the baseline sample, Sherpa yields fewer events in the bulk region resulting in a flatter distribution. The transverse momentum of the leading jet[1] looks similar to the p_T of the Z and $t\bar{t}$ system. It is representative for the transverse momentum of the 2nd, 3rd and 4th leading jet, which also look to be consistent.

Polarisation information from the Z boson is transmitted to the daughter particles q_1, q_2. The polarisation is experimentally accessible through their opening angle $\Delta R(q_1, q_2)$ and reveals characteristics of the weak tZ coupling. To obtain the opening angle, jets on particle level need to be matched to the quarks on parton level. All jets j_i within $\Delta R(j_i, q) < 0.3$ of either quark $q = q_1, q_2$ are considered. If only one jet j_i meets the criterion, the event is dismissed for this comparison. If more than two jets are matched, the jet pair with invariant mass closest to the Z boson mass is chosen. These jets are used for the $\Delta R(j, j)$ distribution. This procedure implicitly assumes that radiation corrections deflect the majority of jets by less than 0.3.

Figure 5.9 displays the $\Delta R(j, j)$ of two jets coming from the Z boson. The anti-k_T jet algorithm makes the presence of two jets within $\Delta R(j, j) < 0.4$ unlikely. The distribution has a maximum at about 1, decreases steadily and drops at values around 3. The sharp rim emerges, because the $\Delta\phi$ contribution is roughly uniform up to values of π. The different simulations generate similar distributions for this variable. MG5_aMC+Py8 NLO produces slightly higher values than the baseline sample and Sherpa yields even higher values. This phenomenon can be explained with the Z boson p_T. Higher transverse momenta of the baseline sample correspond

[1] Jets are numbered according to transverse momentum starting with high momenta.

to a smaller opening angle ΔR of the resulting quarks. On the other hand, the different spin treatment can also have an influence.

MC validation is inseparably connected with the question of consistency. So far, coinciding distributions have been an indicator for well-understood processes and reasonable modelling. This changes when spin effects are analysed. Mismatch of generator predictions is expected because their spin treatment is different. The baseline setup does not consider polarisation of particles after $t\bar{t}Z$ production, while the other two samples take this effect into account with MadSpin or internally in Sherpa.

In bare $t\bar{t}$ production, the spins of the top quarks are correlated through the production mechanism. As the spins influence the kinematics of the decay particles, the spin correlation can experimentally be measured. So-called spin analysers provide information about the correlation C. It is defined as

$$C = \frac{N(\uparrow\uparrow) + N(\downarrow\downarrow) - N(\uparrow\downarrow) - N(\downarrow\uparrow)}{N(\uparrow\uparrow) + N(\downarrow\downarrow) + N(\uparrow\downarrow) + N(\downarrow\uparrow)}$$

where $N(\uparrow\uparrow)$ stands for events with two spin-up top quarks. The correlation ranges from -1 for anti-correlated to $+1$ for correlated spins. Extensive studies have been performed for $t\bar{t}$ production resulting in theoretical predictions and experimental confirmation. An elaborate summary can be found in Ref. [3].

In a similar manner, for $t\bar{t}Z$ production, the spins are expected to be correlated. In analogy to the $t\bar{t}$ case, spin analysers can be defined to quantify the correlation of both top quarks after Z boson radiation. The analysers are illustrated in Figure 5.10. The top quark direction of flight in the $t\bar{t}$ system is chosen as spin quantisation axis as indicated by the blue arrow. In the top quark rest frame, θ_+ is defined as angle between the spin axis and the charged lepton. In hadronic decays, the positive lepton is substituted by the down-type antiquark. Equivalently for the antitop quark, the angle θ_- is spanned by the spin axis and the negative lepton or down-type quark, respectively.

Kinematic considerations allow the correlation [70] of both top quark spins to be approximated by

$$C = -\frac{9 < \cos(\theta_+)\cos(\theta_-) >}{\alpha_+\alpha_-}. \tag{5.1}$$

The analysing powers α_+ and α_- depend on the spin analysers in the top and antitop system. They are given by $\alpha_\ell = 0.998$ [71] and $\alpha_{d/s} = 0.966$ [72] for leptonic and

hadronic decays. For pure $t\bar{t}$ production, the SM predicts[2] $C = 0.33$ [74]. The quoted values are calculated at NLO in QCD.

The correlation is changed in $t\bar{t}Z$ processes by the additional production of a Z boson. While $t\bar{t}$ is predominantly produced by gluon fusion, a plain SHERPA LO simulation indicates that $t\bar{t}Z$ only arises to approximately 65% from gluon fusion. The impact on spin correlations can be assessed using calculations for the Tevatron. These computations predict a correlation of $C = -0.35$ [74]. The flipped sign can mainly be ascribed to the 85% [3] share of $q\bar{q}$ annihilation. Thus, it is reasonable to assume that a higher contribution of $q\bar{q}$ annihilation decreases or even flips the correlation for $t\bar{t}Z$ production.

Z production itself also changes the correlation. If the Z boson is produced in FSR, it couples to the top quark. The weak neutral current couples preferably to left-handed top quarks, but not exclusively. This means that even in the relativistic limit all spin configurations can occur, as long as they obey total spin conservation. Qualitatively, Z boson radiation involves one top quark with some random component and leaves the other top quark unchanged. Therefore, FSR of a Z boson will certainly decrease the absolute correlation $|C|$ with respect to the mere $t\bar{t}$ case.

No quantitative theory predictions about spin correlations in $t\bar{t}Z$ events are found at the time of this thesis. The simulation result can be seen in Figure 5.11 showing the variable $\cos(\theta_+)\cos(\theta_-)$ for every event. The symmetric distribution of the MG5_aMC+PY8 LO setup is consistent with disregarding spin effects in top decays. The other two simulations are asymmetric and agree with each other indicating that spin correlations are correctly taken into account. Averaging over the distributions and using equation (5.1), the correlation C can be estimated. The numerical results and their statistical errors are listed in Table 5.4. They predict that top quark spins are anticorrelated in $t\bar{t}Z$ events. Furthermore, they imply that the absolute correlation is smaller than for $t\bar{t}$.

[2]This result is obtained for calculations at $\sqrt{s} = 14$ TeV. However, it is not expected to change a lot for 13 TeV. For reference, the correlation prediction at 8 TeV is $C = 0.32$ [73].

Generator	Order	Spin preserved	Correlation C
MG5_aMC+Py8	LO	no	-0.006 ± 0.015
Sherpa	LO	yes	-0.213 ± 0.003
MG5_aMC+Py8	NLO	yes	-0.211 ± 0.01

Table 5.4.: The spin correlation of the two top quarks in $t\bar{t}Z$ events is calculated from different simulations. The baseline setup is in agreement with 0 as expected. The spin-considering setups yield consistent values. Uncertainties are derived from statistical uncertainties of the MC datasets.

5.2.3. Kinematic Distributions at 8 and 13 TeV

During Run 1, the analysis aiming at $t\bar{t}Z$ observation was developed for proton collisions at 8 TeV. With increasing centre-of-mass energy, differences in kinematics of final-state objects are expected. Thus, the analysis needs to be optimised to 13 TeV data. In order to estimate qualitative and quantitative changes, the established framework proves useful to compare simulations at different centre-of-mass energies.

Commonly, increased momenta of colliding protons have two major kinematic implications. There are more events with higher total energy available and therefore decay particles are more energetic. In terms of observables, this translates to higher transverse momenta of all kinds of particles. Another consequence of higher energies is that collisions become more asymmetric. To produce the $t\bar{t}Z$ final state, at least the energy corresponding to the particle masses $s = (2m_t + m_Z)^2$ must be available. The interacting partons can contribute different momenta. At higher centre-of-mass energies, partons with a lower momentum fraction x exceed the threshold. This effect should manifest itself in higher $|\eta|$ values.

Cross sections also strongly depend on the collision energy. As more particles with relatively low energies can initiate a hard interaction, typically the cross section increases with the energy. This feature is well understood and shall not be investigated here. Hence, all following distributions are normalised to unity. The MG5_aMC+Py8 NLO setup is used to generate samples and is summarised in Table 5.5.

Kinematic variables related to the $t\bar{t}Z$ process and jet observables are displayed in Figure 5.12 and compared between 8 TeV and 13 TeV. The transverse momentum of the $t\bar{t}Z$ system is shifted to higher values, because more energy is available for ISR. The recoil is reflected in the $t\bar{t}Z$ p_T.

As described above, collisions tend to be more asymmetric at higher energies due to PDFs. Therefore, more events are expected to possess higher absolute pseudorapidities $|\eta|$ of the $t\bar{t}Z$ system. In particular, the increased contribution of gluon fusion, as estimated in Table A.1 in the appendix, supports this assumption. The corresponding plot in Figure 5.12 disagrees with this intuitive reasoning. It

Generator	Order	Process	Energy $\sqrt{s}$	Cross section [fb]
MG5_aMC+Py8	NLO	$t\bar{t}Z \to q\bar{q}$	8 TeV	138.58
MG5_aMC+Py8	NLO	$t\bar{t}Z \to q\bar{q}$	13 TeV	538.42

Table 5.5.: Events of the $t\bar{t}Z$ process are generated based on the NLO MG5_aMC+Py8 setup. Only $Z \to q\bar{q}$ are generated on parton level. Two different centre-of-mass energies are simulated, namely 8 TeV and 13 TeV.

shows no significant difference between 8 and 13 TeV distributions. A possible physical explanation is that the increased p_T of the $t\bar{t}Z$ system precisely compensate the effect of asymmetric collisions. The $t\bar{t}Z$ final state involves three particles with high masses. It is therefore produced relatively close to the energetic threshold even in 13 TeV collisions, which could cause the η distribution not to change substantially. It is worth noting that the same behaviour is observed in simulations of $t\bar{t}H$ processes. A further investigation of this phenomenon would help to better understand the $t\bar{t}Z$ kinematics.

Figure 5.13 shows that the $\Delta R(q, q)$ distribution of quarks created in the Z boson decay changes from 8 to 13 TeV. The quarks move closer together in the $\eta-\phi$ plane. Smaller values are favoured, because the Z boson is more energetic. Thus, the quark pair is boosted in the Z boson direction of flight to a higher degree. This characteristic distribution can contribute to signal identification at higher collision energies. In particular in leptonic Z boson decays, which are expected to look similar, the $\Delta R(\ell^+, \ell^-)$ could help to identify the boosted Z boson and reject background events.

Observables on particle level are shown in Figure 5.14. The transverse momentum of the leading jet has higher values in 13 TeV collisions and exceeds the low-energetic simulation above 150 GeV. In addition, the jets are more in the forward η regions. This qualitative behaviour perfectly agrees with expectations. It is similar for the 2nd, 3rd and 4th jet.

The jet multiplicity in Figure 5.15 includes all $t\bar{t}$ decay modes and has therefore higher values than the corresponding plot in Figure 5.8. The large share of all-hadronic decays increases the jet multiplicity on average. When comparing the different centre-of-mass energies, jets carry more transverse momentum at 13 TeV and therefore more low-energetic jets pass the p_T cut. In addition, more radiation occurs on parton level due to higher available energies. This is visible in the high multiplicity region, where the 13 TeV simulation is more abundant. The absolute discrepancy at low jet numbers is small. The relative difference comes from the $|\eta| < 2.5$ cut rejecting jets with high pseudorapidities. In conclusion, the two effects of higher transverse momenta and pseudorapidities effectively create more jets on average and simultaneously smear the distribution.

In $t\bar{t}Z$ analyses, the events have been categorised according to jet and b-jet multiplicities. The presented comparison suggests that this region definition can be reoptimised for 13 TeV analyses. Potentially, higher multiplicities with a better signal-to-background ratio become statistically relevant.

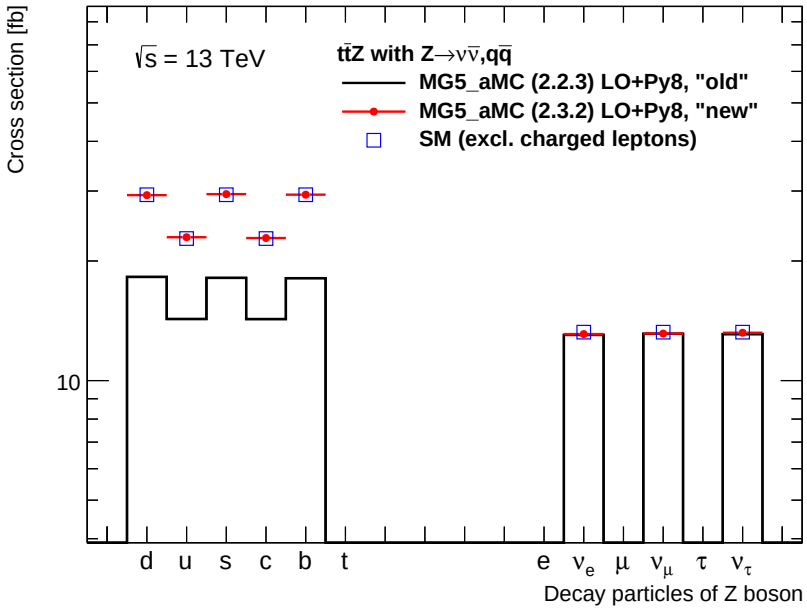

Figure 5.3.: Cross section of ttZ production split up according to the Z decay particles representing the branching ratios. Two simulations with baseline setup are shown with Z decay into $\nu\bar{\nu}$ and $q\bar{q}$. The corrupted sample ("old") contains a bug related to `CKKW-L` merging. This is reflected in the Z decay. The fixed sample agrees with the SM values calculated in the massless limit.

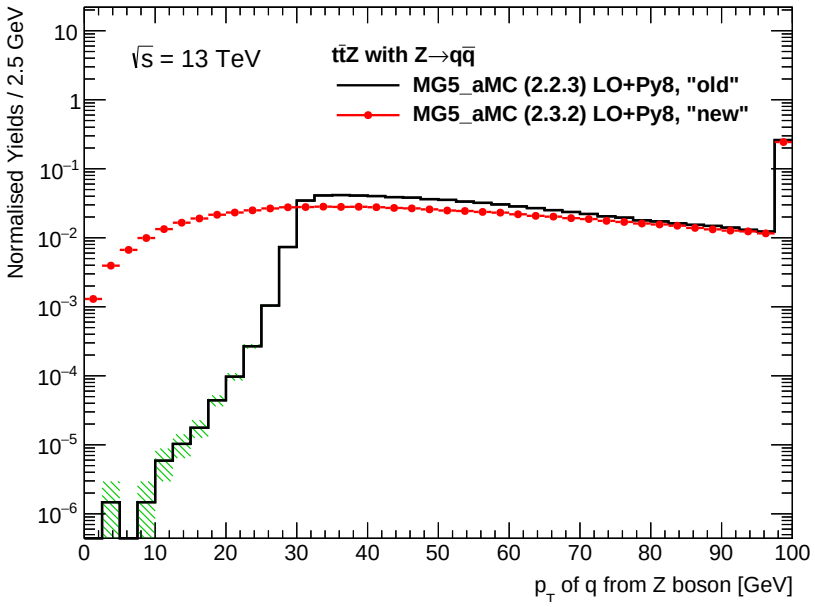

Figure 5.4.: Transverse momentum of the quark created in the Z boson decay. In the old sample, values below 30 GeV are suppressed, because the merging algorithm erroneously removes them. The regenerated simulation behaves as expected. The distribution of the corresponding antiquark exhibits the same features. Values over 100 GeV are added to the last bin. Decays of Z bosons to neutrinos are rejected on parton level using information of the MC truth record.

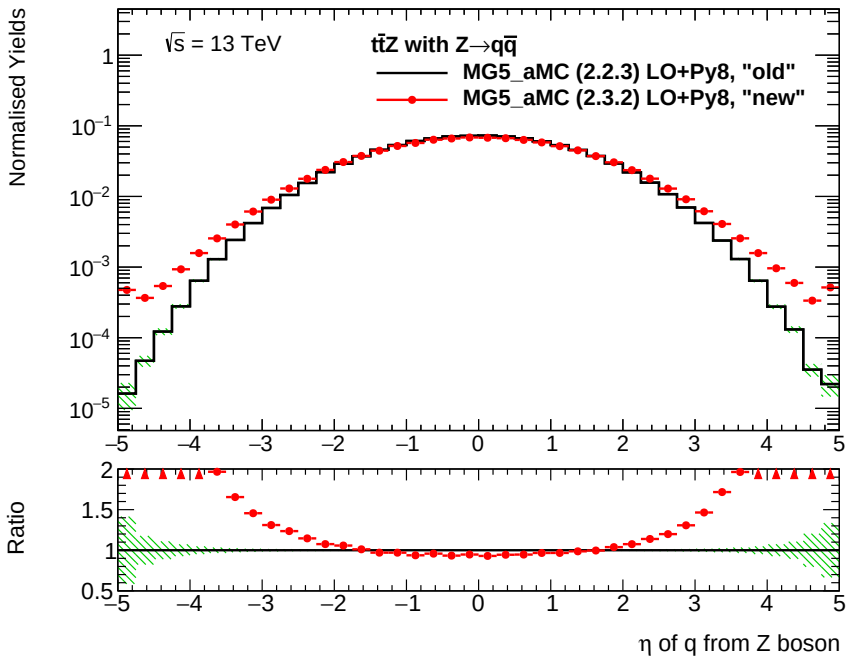

Figure 5.5.: The pseudorapidity of quarks from the Z boson decay is shown comparing the corrupted and corrected simulation on parton level. The absolute pseudorapidity has higher values in the revised sample, which fits to the changes introduced by the merging algorithm. Decays of Z bosons to neutrinos are rejected on parton level using information of the MC truth record. Errorbars represent statistical errors in the MC samples.

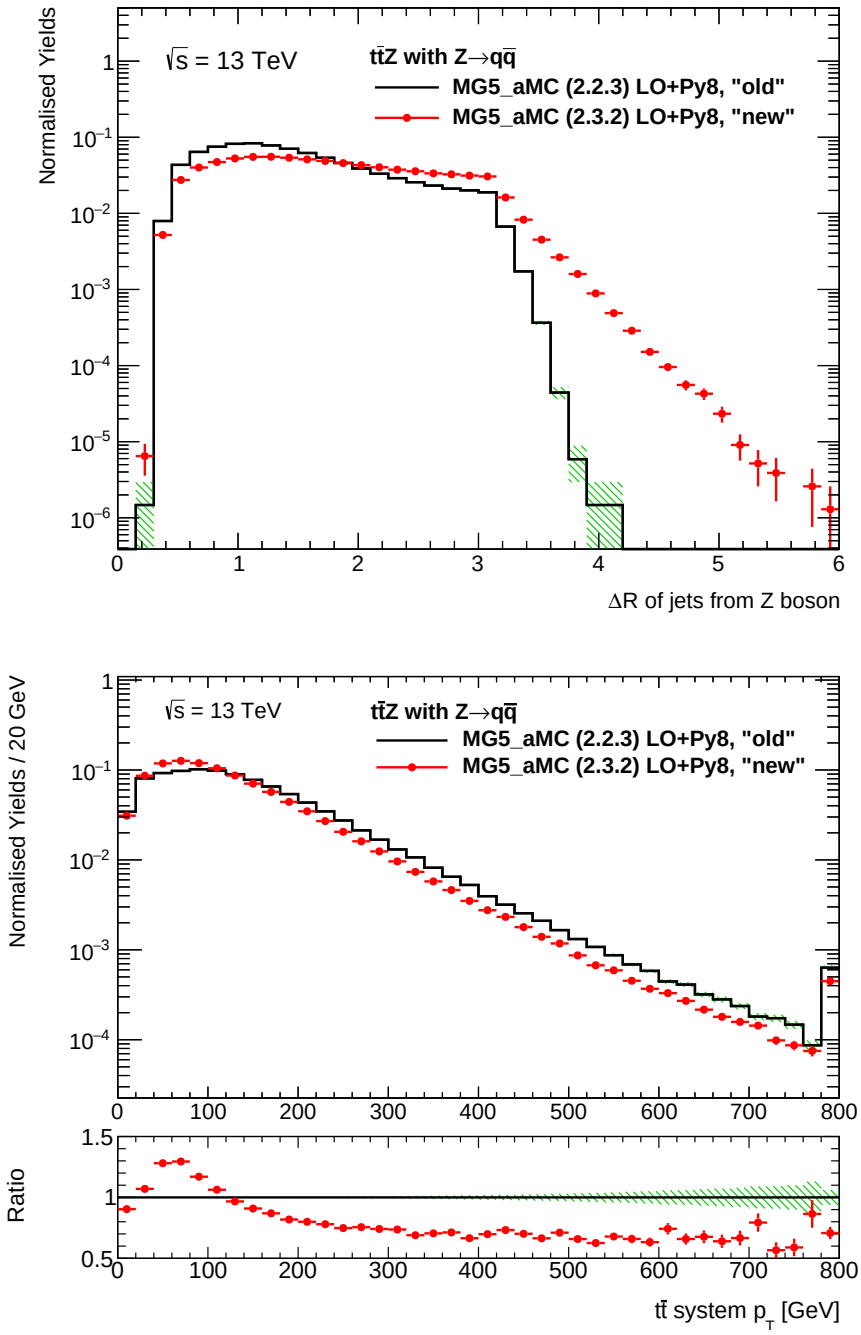

Figure 5.6.: The same simulation is shown as in Figure 5.5. The $\Delta R(j, j)$ distribution mostly occupies values up to π, because of the quite uniform $\Delta\phi(j, j) < \pi$ contribution. The revised simulation creates larger opening angles. It also predicts more events with smaller transverse momentum of the $t\bar{t}$ system. No acceptance cuts are applied for jets in the top plot.

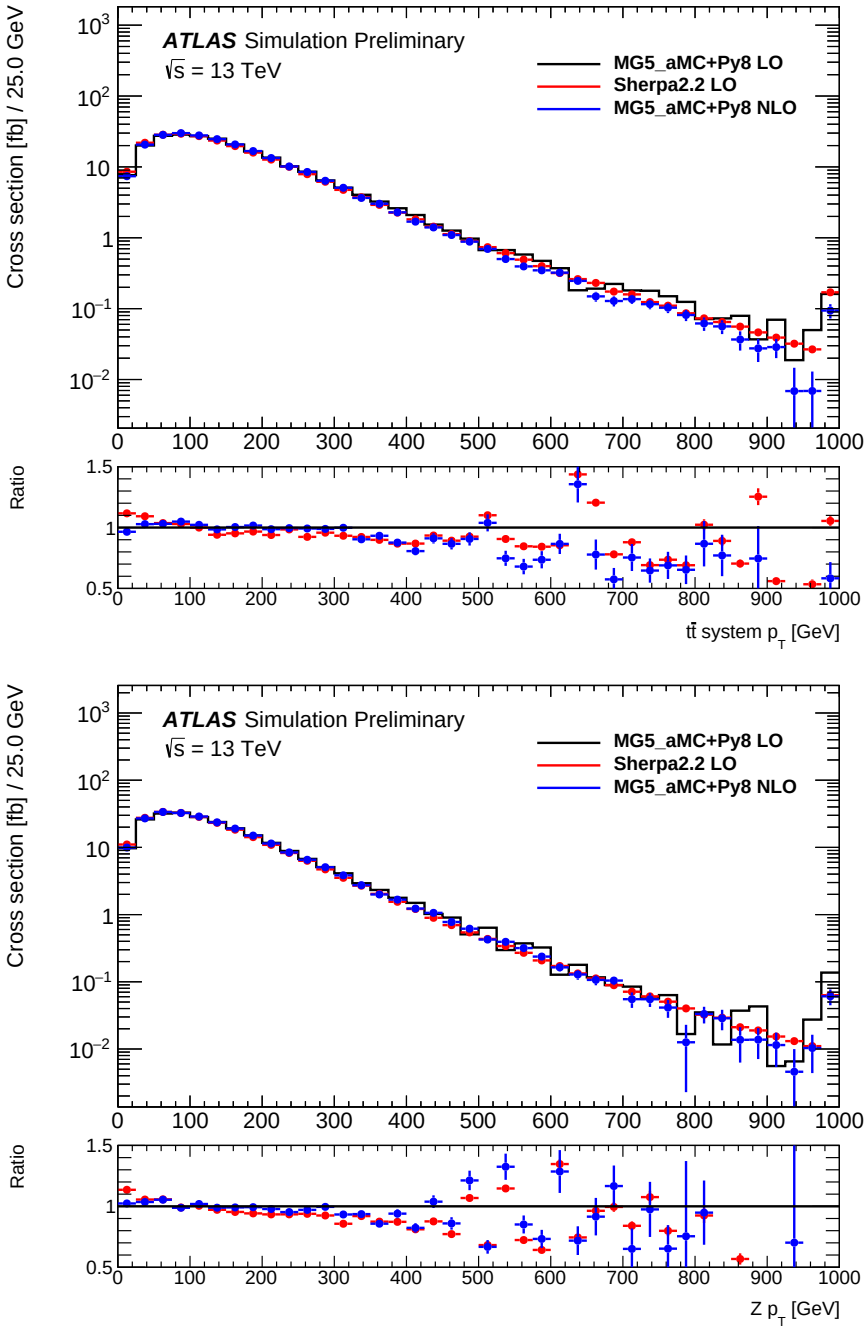

Figure 5.7.: Two kinematic variables in $t\bar{t}Z$ simulations on parton level [60]. They are related through recoil and show a similar behaviour. MG5_aMC+Py8 LO systematically generates higher transverse momenta compared to Sherpa and NLO MG5_aMC+Py8. In particular for the Z boson, higher statistics would be needed for a meaningful statement. Both distributions do not show statistical errors for the baseline sample. Other errorbars represent statistical errors in the MC samples.

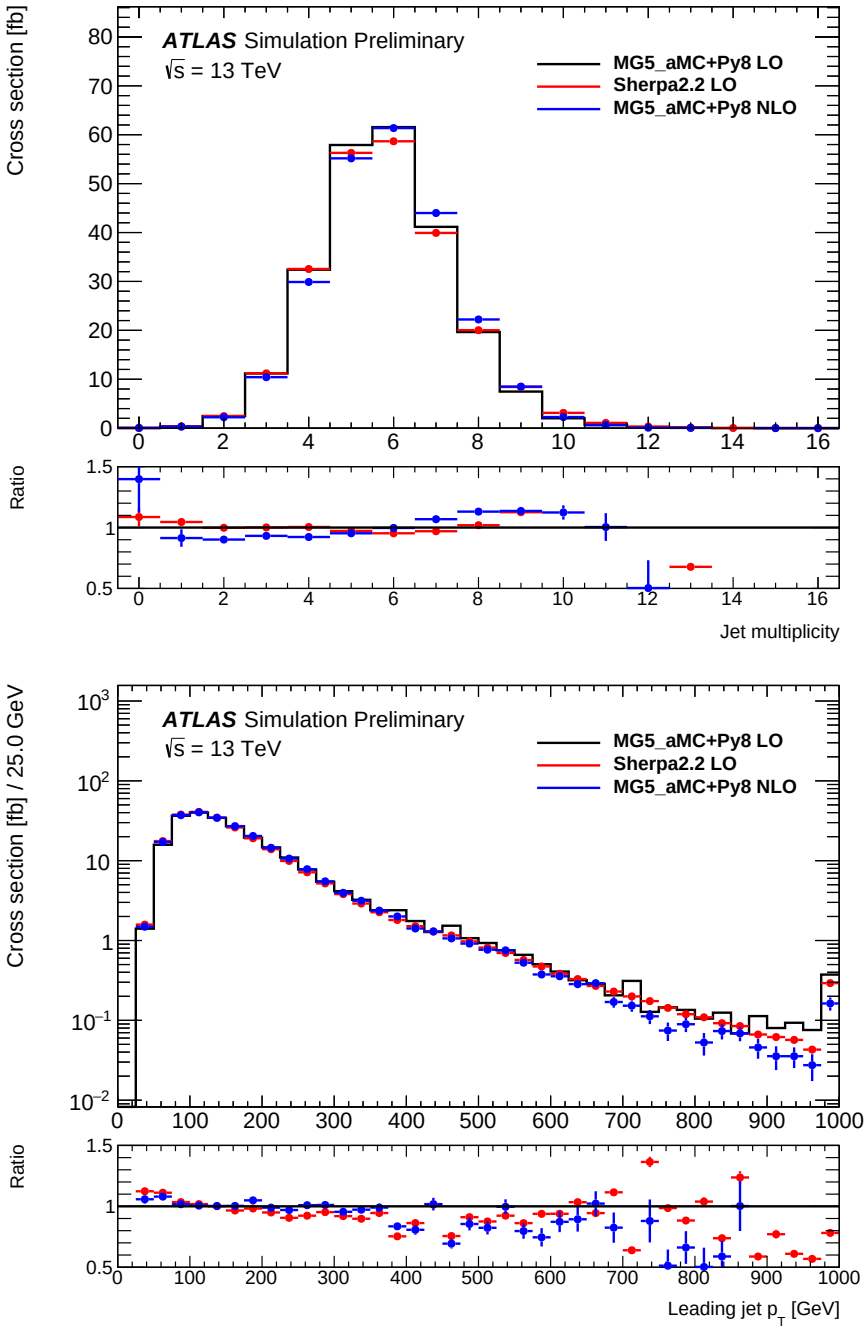

Figure 5.8.: Two particle level distributions related to jets [60]. The jet multiplicity in SHERPA is similar to the baseline sample, but has slightly more ouliers. MG5_aMC+PY8 NLO shows a clear trend to higher multiplicities. In the transverse momentum of the leading jet, the two MG5_aMC+PY8 samples agree well up to values of 350 GeV. Above that, the same behaviour as in other p_T distributions is visible. The plots do not show statistical errors for the baseline sample.

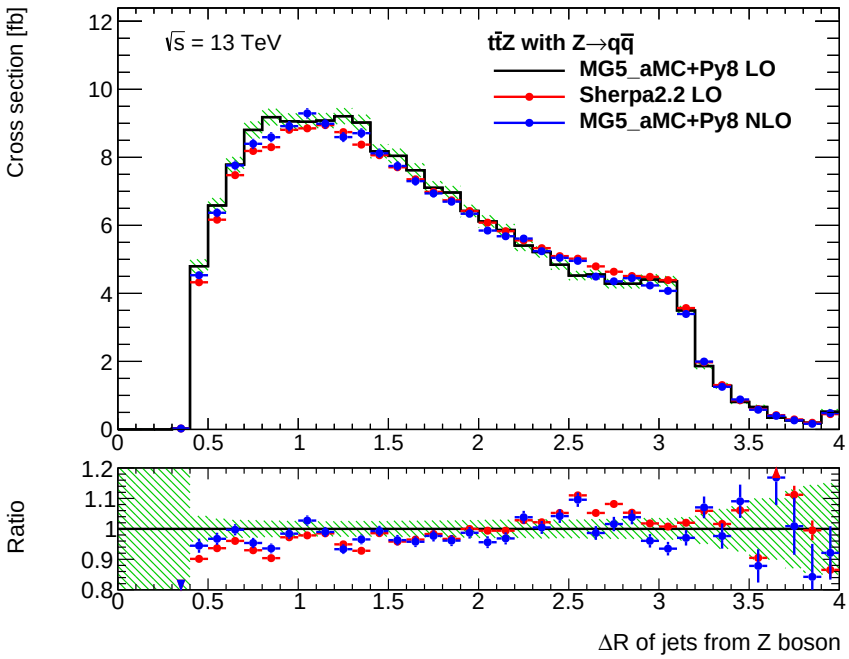

Figure 5.9.: Compared to the baseline sample, the distance parameter ΔR between jets assigned to the Z boson is shifted to higher values for MG5_aMC+Py8 NLO and even higher values for Sherpa. No object cuts are applied for jets.

Figure 5.10.: The top quark and its leptonic (left) and hadronic (right) decay in the top quark rest frame. The down-type fermion from the W decay serves as spin analyser. Its direction of flight spans the angle θ with respect to the helicity axis.

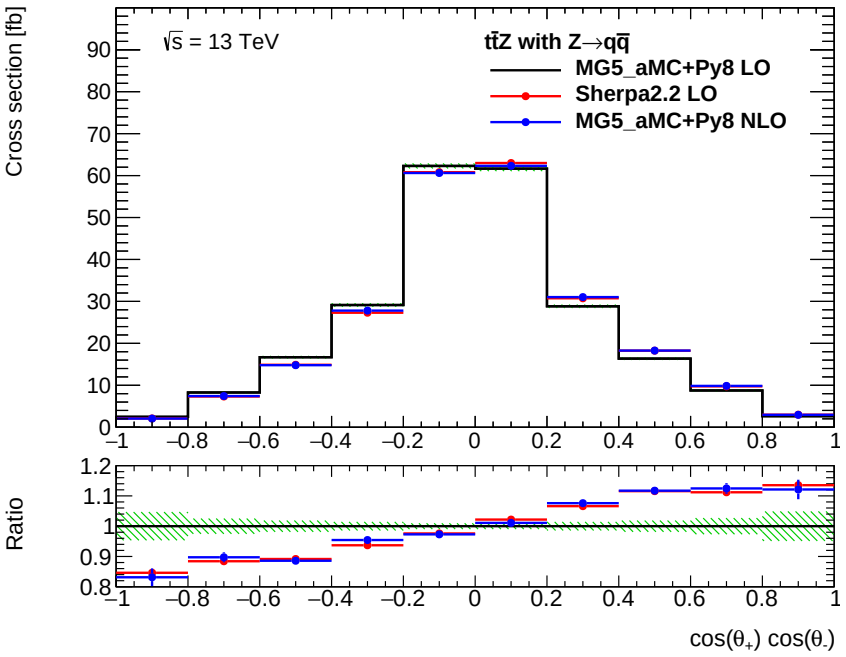

Figure 5.11.: The distribution $\cos(\theta_+)\cos(\theta_-)$ is sensitive to $t\bar{t}$ spin orientations. The baseline sample ignores spins and predicts a symmetric shape. The other two simulations conserve spins for the $t\bar{t}$ decay products and yield consistent, asymmetric distributions.

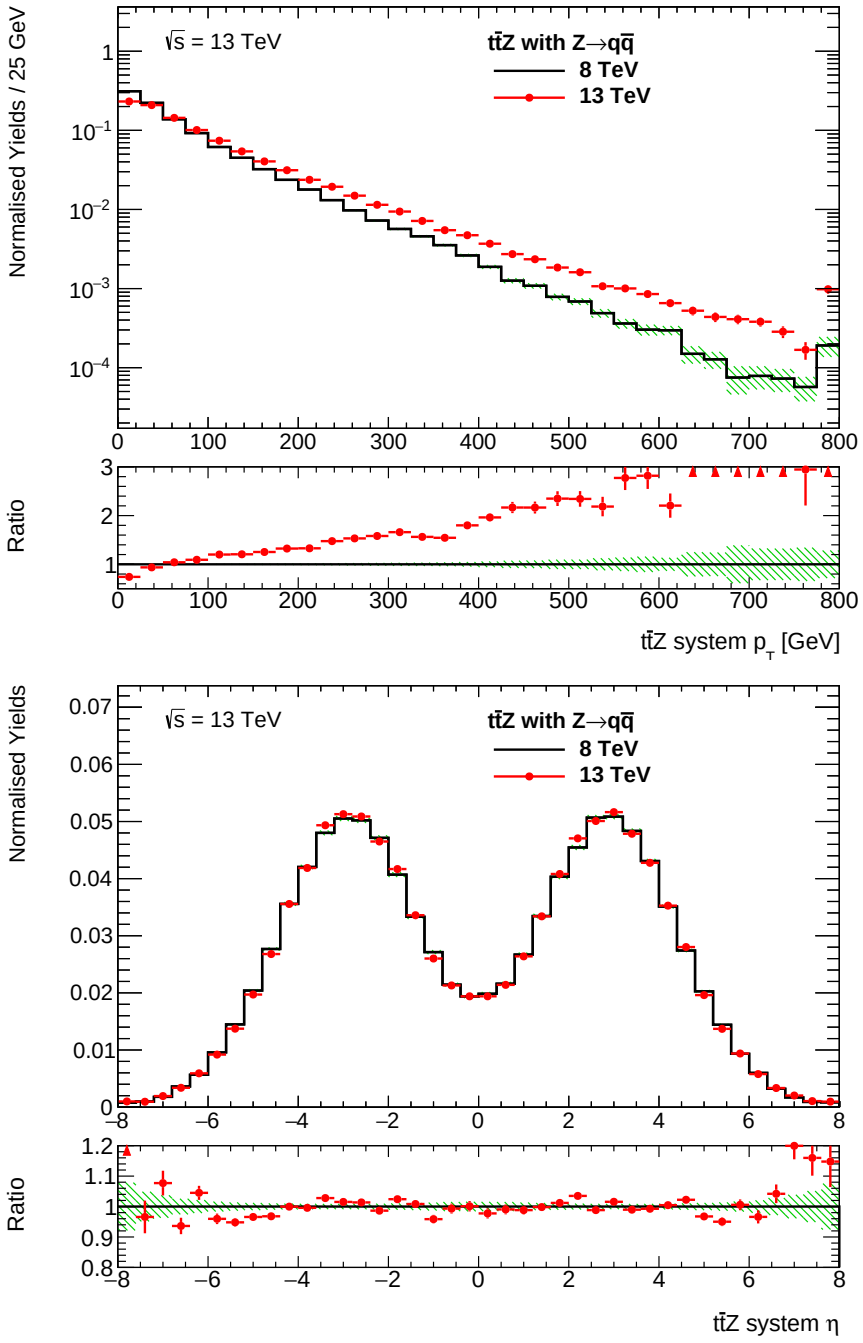

Figure 5.12.: Variables on parton level are depicted for $t\bar{t}Z$ production at different energies. All distributions are normalised to unity. The $t\bar{t}Z$ transverse momentum is higher at 13 TeV. No significant difference is visible in the pseudorapidity distribution.

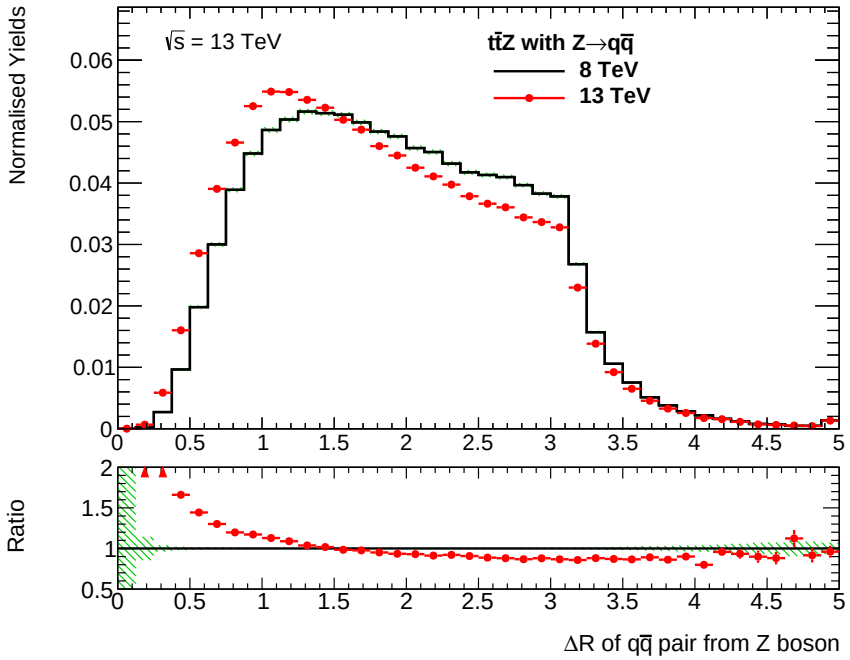

Figure 5.13.: At 13 TeV, the variable $\Delta R(q, q)$ could contribute to separate signal and background processes. Due to higher Z boson momenta, the distribution takes a more characteristic shape and could prove beneficial in a MVA.

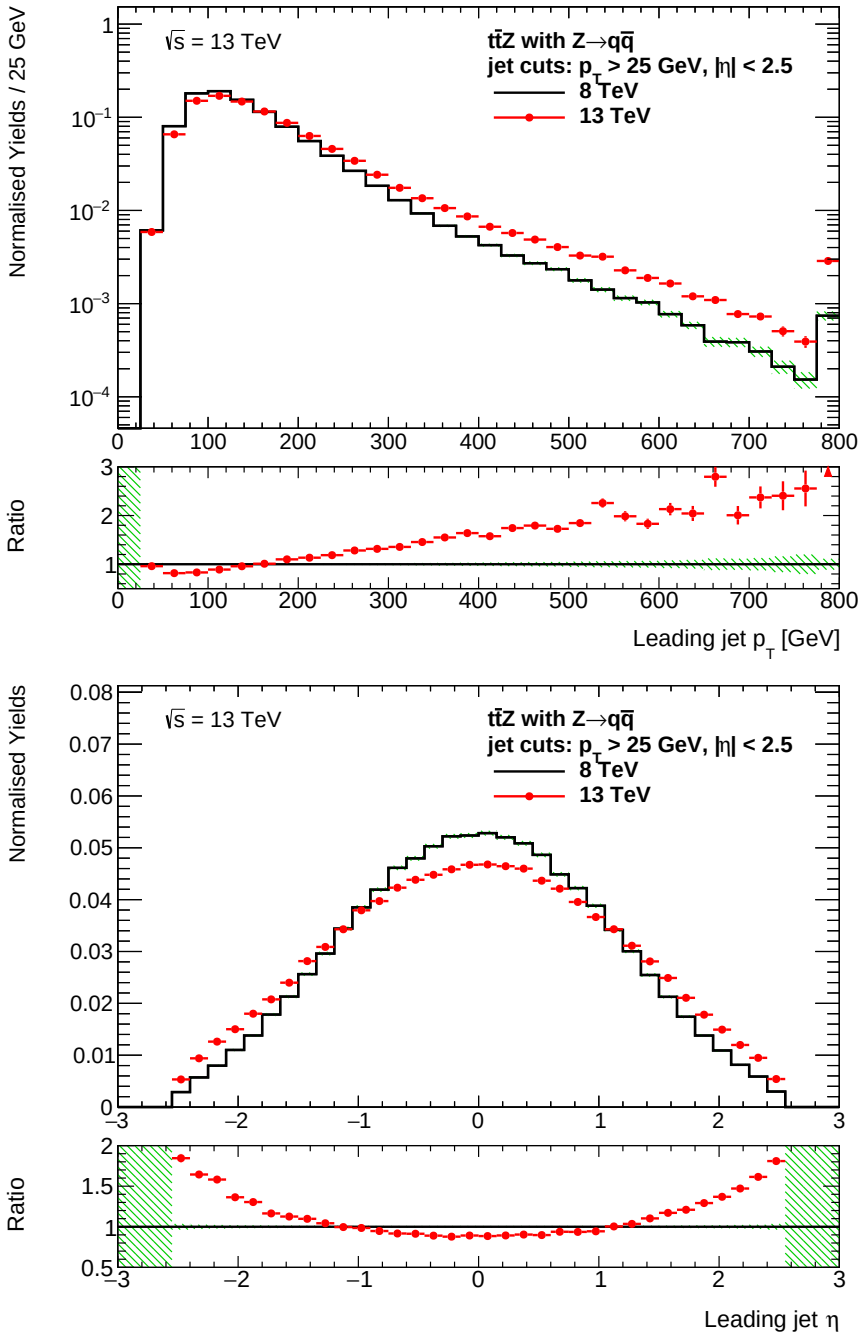

Figure 5.14.: Normalised jet observables at 8 TeV and 13 TeV. In more energetic collisions, jets receive higher transverse momenta. This is exemplarily shown for the leading jet, whose p_T is shifted to higher values. More asymmetric interactions boost events along the beam axis and consequently jets obtain higher pseudorapidities.

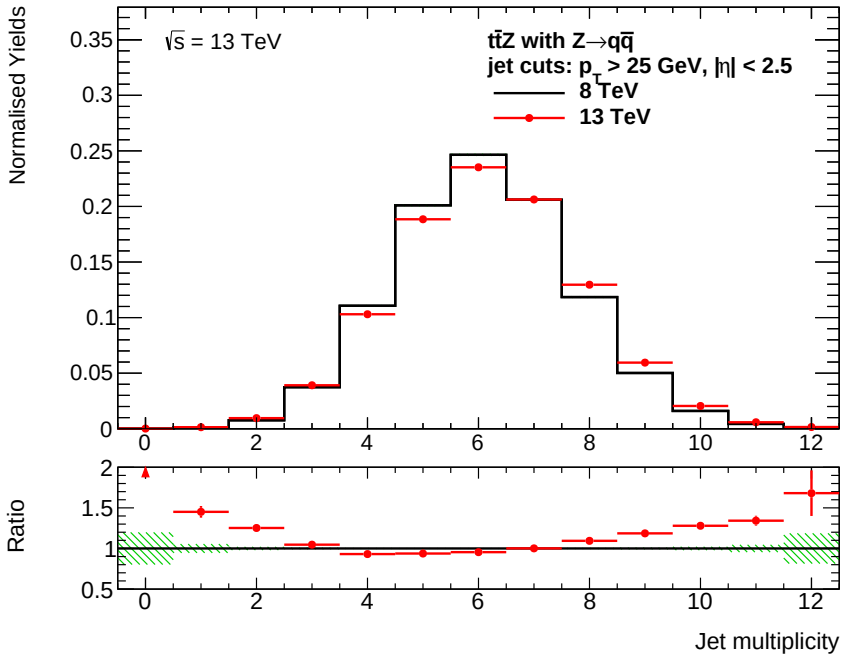

Figure 5.15.: The jet kinematics have an impact on the jet multiplicity. More jets pass the p_T cut and simultaneously more jets fail the $|\eta|$ cut. The first effect outweighs the latter so that on average more jets are created.

6. Multivariate Analyses

Compared to other processes at the LHC, $t\bar{t}V$ production occurs rarely. A major challenge in its measurement is the small signal-to-background ratio S/B. The relevant backgrounds depend on the signal signature, which is mainly driven by the number of charged leptons. Hence, the observed signatures are split up into a dilepton, trilepton and tetralepton channel. For $t\bar{t}Z$ production, the latter channel has a high S/B, but suffers from low statistics. Dileptonic events, conversely, can be produced in various $t\bar{t}Z$ decays, but suffer from low yields with respect to backgrounds. The trilepton channel combines the strengths and weaknesses of the other two channels and proved to be most significant in the 8 TeV analysis.

The dilepton channel is worth studying because it is most sensitive to $t\bar{t}W$ production. Thus, it can profit from combining the measurement of $t\bar{t}W$ and $t\bar{t}Z$. In addition, its high statistics can be exploited with statistical methods to enhance the signal-to-background ratio. This chapter focuses on the final state with two leptons of opposite sign (2ℓOS), whose invariant mass is within a 10 GeV window around the Z boson mass.

In this channel, the largest background comes from the dileptonic decay of top quark pairs. As estimated in Table 6.1, the signal is expected to be lower by a factor of about 10^{-3} with respect to $t\bar{t}$. The table suggests that a measurement of $t\bar{t}Z$ processes could be more sensitive at 13 TeV compared to 8 TeV, while the S/B deteriorates for $t\bar{t}W$. Also other backgrounds play a role. A large contribution is

Process	Cross section ratio 8 TeV	13 TeV
$\frac{\sigma_{t\bar{t}W^+} + \sigma_{t\bar{t}W^-}}{\sigma_{t\bar{t}}}$	$1.2 \cdot 10^{-3}$	$0.9 \cdot 10^{-3}$
$\frac{\sigma_{t\bar{t}Z}}{\sigma_{t\bar{t}}}$	$1.1 \cdot 10^{-3}$	$1.2 \cdot 10^{-3}$

Table 6.1.: Suppression of the $t\bar{t}V$ processes with respect to $t\bar{t}$ at $\sqrt{s} = 8$ TeV and 13 TeV in the 2ℓOS channel. The 8 TeV values are taken from ($t\bar{t}V$ [45, 75], $t\bar{t}$ with the same framework as for 13 TeV computations).

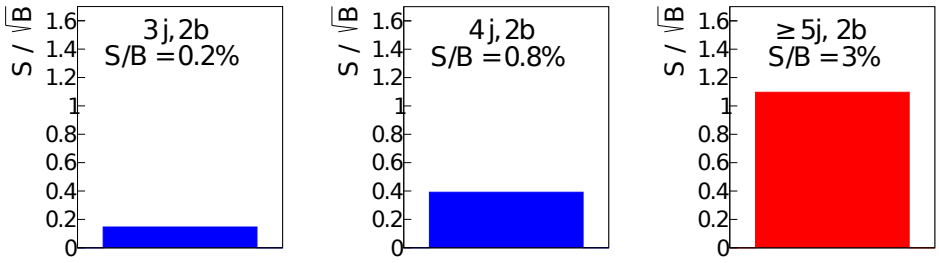

Figure 6.1.: Signal-to-background ratio in the Z window of the 2ℓOS channel [77]. On parton level, 6 jets are expected from the all-hadronic $t\bar{t}$ decay. Regions are shown with 3, 4 and more than 4 jets. Two of the jets have to be b-tagged. Events with $t\bar{t}Z$ serve as signal and $t\bar{t}$ and Z + jets as background.

expected from Z + jets, diboson and single top events, as estimated for the analysis at 8 TeV [76]. A rare process with a similar signature is $t\bar{t}H$.

To increase the S/B, events are commonly classified according to the number of jets and b-tagged jets. The region with 5 or more jets, of which 2 or more are b-tagged, is comparatively sensitive to $t\bar{t}Z$, as indicated in Figure 6.1. To further filter the 3% signal events from the remaining backgrounds, multivariate analyses (MVAs) are a powerful tool. Their concept and the application in $t\bar{t}V$ processes are presented in this chapter.

6.1. Concept of MVAs

To visualise how multivariate analyses (MVA) [78, 79] work, Figure 6.2 illustrates scatter plots of signal (red) and background (blue) events. The axes x_1 and x_2 show variables from the event, for instance the transverse momentum of one particular lepton or its pseudorapidity. Cuts can be applied trying to discriminate signal and background. Rectangular cuts can prove beneficial, but other, more sophisticated selection criteria may be more efficient.

In terms of event classification two kinds of errors can be made. Background events are mistakenly reconstructed as signal (type I error, occurs with probability α) or signal events are rejected (type II error, occurs with probability β). The signal efficiency is defined as $\epsilon = 1 - \beta$ and the background rejection as $R = 1 - \alpha$. Thus, the aim is to find a classification as close as possible to $\epsilon = R = 1$.

The approach of MVAs is to make use of a multi-dimensional observable space instead of applying one- or low-dimensional cuts consecutively. Mathematically, an MVA maps a d-dimensional variable space to a real number $y \in \mathbb{R}$. A constant value of $y = c$ corresponds to a hypersurface splitting the d-dimensional space into two

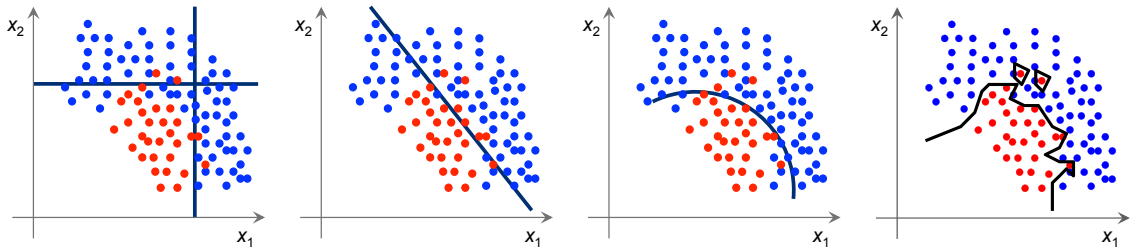

Figure 6.2.: Scatter plot of signal and background events. Simple, rectangular cuts are applied on the left and become more sophisticated to the right-hand side. MVAs can help to find efficient cuts separating signal and background. The rightmost plot illustrates that MVAs can become sensitive to statistical fluctuations. This effect is called overtraining.

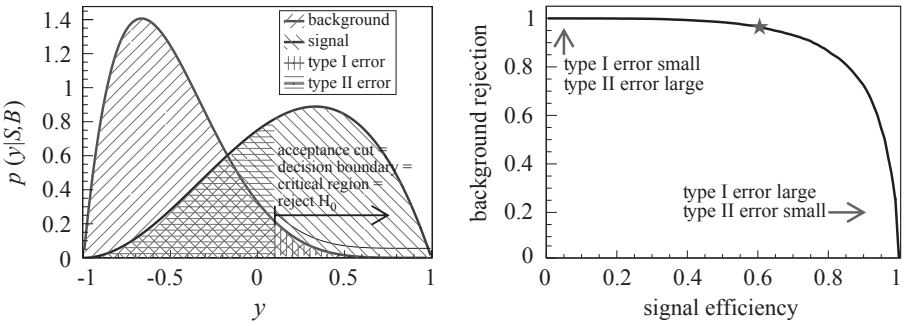

Figure 6.3.: A MVA assigns every event a value y. The left Figure shows the probability density of an event to be signal or background as a function of y. In this example all events with $y > 0.1$ are accepted as signal events. Every cut on y corresponds to one point in the right diagram. A star represents the cut of $y > 0.1$.

regions. To select all events that lie in one of the regions, a one-dimensional cut like $y > c$ can then be applied. To choose an appropriate selection, it is helpful to display the amount of signal and background events as a function of y, as depicted in Figure 6.3. The right plot illustrates, how background rejection and signal efficiency depend on the cut value. It is called receiver-operating-characteristic (ROC). The ROC integral is commonly used to assess the discrimination power of the MVA output variable [80].

When many variables are used, it becomes difficult to construct an efficient MVA mapping by hand. Instead, supervised machine learning can be used. Signal and background processes are simulated and passed on to a learning algorithm. This learning algorithm classifies the events, compares the result to the genuine information and modifies the classification accordingly. This procedure is repeated multiple times until the algorithm gives suitable results. Afterwards, the trained algorithm is tested with different signal and background events. These events may

be generated with the same method, but have to be independent from the training events. This is a suitable test for overtraining. Finally, the algorithm can be used to separate signal-like and background-like events in data recorded in experiments.

6.2. Artificial Neural Networks

Inspired by biological networks, artificial neural networks are frequently used as machine learning algorithm. Compared to nature, however, artificial neural networks are rather primitive and have only very few nodes. Every network consists of nodes and edges. The nodes have a set of properties and can interact via edges. Edges carry a weight indicating how large their influence is. For machine learning purposes usually networks without loops, so-called feed-forward networks or multi-layer perceptrons (MLP), are used.

An example of an MLP is shown in Figure 6.4. The left layer has one node per input variable x_i. The values of these input variables are forwarded to the hidden layer along edges represented by arrows. The edge weight is indicated by the values w_{ij}. In this example only one hidden layer is depicted, but multiple hidden layers can be used in general, each with an arbitrary number of nodes. At the end, all the information is combined into one output variable y (see Figure 6.3).

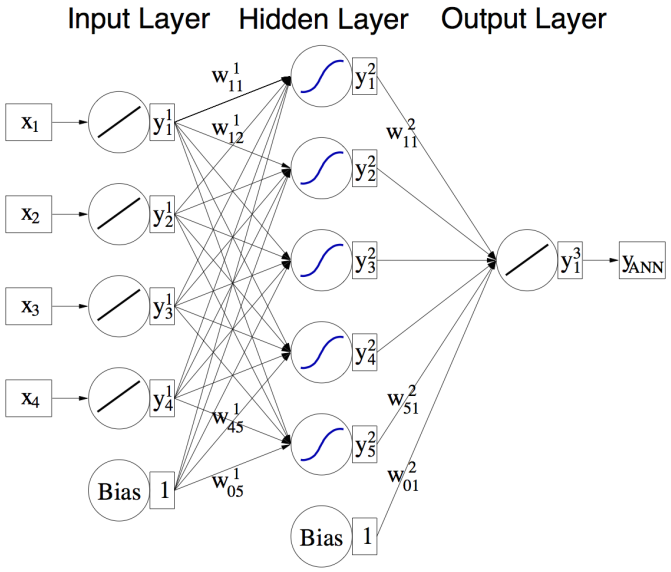

Figure 6.4.: Feed-forward network with one hidden layer.

The values of the input nodes are taken from the physical variables of the event. The value of node j in a subsequent layer n is defined by

$$x_j^n = f\left(\sum_i w_{i,j}^n x_i^{n-1} + w_{0,j}^n\right),$$

where the sum loops over all nodes i of the previous layer and the additional term $w_{0,j}^n$ represents a bias. The monotonic function f is called activation function. It is mostly taken to be non-linear in order to model complex behaviour.

The "Root Data Analysis Framework" comprises a "Toolkit for Multivariate Data Analysis" (TMVA) [81]. It provides a convenient implementation of numerous MVA techniques. In this report, the MLP function of TMVA is used for $t\bar{t}V$ studies.

6.3. Influence of Hidden Layers

The network structure has a vital impact on the separation power of the framework. To achieve optimal discrimination of signal and background, a proper arrangement of nodes must be chosen. There is, however, no general recipe stating what architecture proves beneficial for a given input dataset. The following discussion is limited to MLPs [79].

Consider an MLP with M input nodes, one hidden layer with sufficiently many nodes N and one output node. This network can approximate any continuous mapping $y(x_1, ..., x_M)$, provided it uses a sigmoidal activation function f [82]. The error of this approximation converges with $\mathcal{O}(\frac{1}{N})$ [83]. This erroneously leads to believe that the network structure is subordinate for applications. But a plain MLP comes at a price, namely a large number of edge weights. Other topologies can be more efficient in the sense that they introduce fewer weights and biases to describe the same mapping. Fewer weights reduce the training time and entail more predictive power, because less bias is introduced. In other words, networks with fewer weights are more flexible. They rely less on delicate features of simulations and might therefore act better on real data.

When training a neural network, the edge weights are iteratively optimised and the employed algorithm has considerable impact on the final discrimination power. In TMVA, so-called "back propagation" is implemented. To train the MLP, simulated events are propagated through the network. The number of iterations per event is denoted as training cycles. A larger number of repetitions improves the result, but saturates at some point, because repeated training with the same data can only yield limited optimisation.

In the following, the influence of the network structure and the number of training cycles is investigated. MC simulations of both $t\bar{t}W$ and $t\bar{t}Z$ are used as signal processes and trained against the dominant background $t\bar{t}$ in the ℓ+jets and dileptonic decay channel. All $t\bar{t}V$ events are first 13 TeV test samples generated in the MC14 production campaign. The generator MG5_aMC was used at LO with the PDF set `CTEQ6L1` and Pythia8. The same PDF is used for the $t\bar{t}$ simulation, which is performed with Powheg [84] and Pythia8. For $t\bar{t}V$ the `AUET2B` tune [85] and for $t\bar{t}$ the `Perugia2012` tune [86] is employed. An overview of the simulations can be found in Table 6.2. The samples are divided into two equal parts, of which one is used for training and one for testing.

DSID	MC process	Cross section [pb]	Raw number of events after cuts
119353	$t\bar{t}W$	0.20145	4,075
174830	$t\bar{t}W$+j	0.13129	
174831	$t\bar{t}W$+jj	0.16274	
119355	$t\bar{t}Z$	0.18575	3,191
174832	$t\bar{t}Z$+j	0.16630	
174833	$t\bar{t}Z$+jj	0.20756	
110401	$t\bar{t}$	695.84	103,366

Table 6.2.: MC simulations used to investigate the influence of the neural network structure. $t\bar{t}V$ processes were generated with MG5_aMC+Py8 LO, $t\bar{t}$ with Powheg+Py8.

For the classification 18 input variables were used mainly considering transverse momentum and angular distributions of jets and leptons. The variable choice is essential for the separation power. Distributions can only contribute to discrimination, if they are sensitive to differences of signal and background processes. The list of used variables can be found in Appendix C. More information about first studies can be found in Ref. [77].

In the 2ℓOS region, events are required to have two leptons (e, μ) with opposite sign. Both leptons must have the same flavour and their invariant mass is supposed to be within a 10 GeV window around the Z boson mass. Events must contain at least 3 jets. The average angular distance of all jet pairs is required to be above $\Delta R_{ave} > 0.75$.

In Figure 6.5, the result of classifications with TMVA is shown in terms of the ROC integral. On the x-axis the number of iteration cycles for training is varied, on the y-axis the network structure is modified. The combination of comma separated

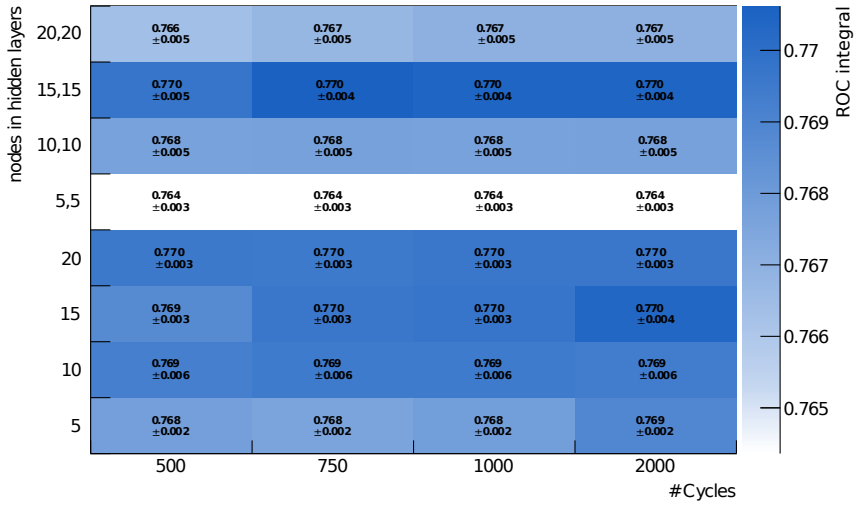

Figure 6.5.: ROC integral for different training iterations (x-axis) and network structures (y-axis). One or two hidden layers were used. The labels on the y-axis indicate the number of nodes in the respective layers. Each cell shows the average ROC integral of 9 classifications with the respective statistical error. For all 9 iterations the data is split into training and testing data in a different way.

values stands for the number of nodes in the (one or two) hidden layers. The colour coding in each cell corresponds to the ROC integral. Also the statistical uncertainty is listed. An ensemble test estimates the uncertainty by splitting the simulation data into training and testing samples in a different way. For different cells, the same set of splittings is used.

At first sight, Figure 6.5 indicates that the ROC integral is quite stable with different training and network choices. The absolute fluctuations are in the order of the statistical error. However, as the same data splitting is applied in all cells, the cell-to-cell variation may be more significant than the uncertainties suggest. Throughout different network structures, a larger number of training cycles yields higher ROC integrals. This might be a hint to investigate the influence of even more iterations. When increasing the number of training cycles, however, it is important to keep an eye on overtraining effects.

The variation of the network structure does not yield a clear picture, although the arrangement of layers shows a larger influence on the ROC integral than the number of iterations. In the case of two hidden layers the integral is smaller than with one layer, except for row $15, 15$. This result, however, is not significant because of the small number of signal events. Only about 3,000 and 4,000 events for $t\bar{t}Z$ and $t\bar{t}W$ were used to train the neural network. No region cuts could be applied due to

the small statistics. These cuts could for example constrain the number of jets or jets with "b-tags".

To assess the effect of overtraining, the Kolmogorov-Smirnov (K-S) test [78] is a helpful measure. It compares the cumulative functions of the training and testing distributions and is sensitive to their maximal difference. A smaller difference indicates better agreement between the two functions and ergo less overtraining. The TMVA implementation returns a value between 0 and 1, where 1 corresponds to good agreement. In a similar fashion as in Figure 6.5 the K-S test results are evaluated. The test values are rather randomly distributed and have similar magnitude as their uncertainties. This fact supports the suggestion that more statistics is needed and that the signal needs to be narrowed down further into different analysis regions.

7. Conclusion and Outlook

Since its discovery in 1995, the top quark properties have been investigated intensively. The weak isospin, however, has never been directly measured. With the energies available at LHC, the suppressed $t\bar{t}Z$ production becomes detectable. Its kinematics are sensitive to the third component of the top quark isospin. Therefore, a precise analysis of this process is able to further constrain the SM.

To test the experimental results against theory expectations, accurate simulations are indispensable. In this thesis, the stepwise development and sanity checks of simulations were presented as well as the datasets validated for physics analyses. A comparison of the kinematics at $\sqrt{s} = 8$ TeV and 13 TeV was shown with focus on the $t\bar{t}Z$ measurement during Run 2. The MC generator MadGraph5_aMC+Pythia8 was used to generate samples at LO multileg and NLO interfaced with Pythia8 for parton shower and hadronisation. One setup with Sherpa v2.2 was also employed at LO multileg.

The setup for MC generation has been further developed and improved towards Run 2. A test of this new setup was presented at 8 TeV for MG5_aMC+Py8 LO and compared with settings from Run 1. A major difference is the change in PDF set from `CTEQ6L1` to `NNPDF2.3LO`. Sound overall agreement is observed suggesting a coherent production. Simulations with `NNPDF2.3` show small systematic deviations with higher transverse momenta and slightly more jets.

At 13 TeV, a bugfix in the interface between MG5_aMC to Py8 was found concerning `CKKW-L` merging. A revised simulation corrects defective features and its predictions correspond to expectations. In particular, the remodelled branching ratio of the Z boson provides a good quantitative comparison with the SM. All kinematic variables are reasonably distributed in the rectified setup.

Thereafter, a comparison of the three generator setups in the ℓ+jets channel of $t\bar{t}$ pairs and hadronic Z boson decay was presented. All generators model kinematic variables similarly. Two trends are apparent despite the rather small statistics of the baseline sample (MG5_aMC+Py8 LO). Various transverse momenta are larger in the baseline sample compared with the other two generators. The predictions in jet multiplicity are similar in the LO simulations and are shifted towards higher numbers in MG5_aMC+Py8 NLO.

The datasets were validated and parts of these studies were documented by the ATLAS collaboration [60]. The modelling efforts did considerably contribute to the first cross section measurement of $t\bar{t}V$ processes at 13 TeV [51].

It is planned to use more sophisticated methods for further analyses of $t\bar{t}V$ processes. To this end, it is helpful to compare the kinematics at 13 TeV with respect to those at 8 TeV. In was shown that identifying Z bosons might become easier and can assist in separating $t\bar{t}Z$ processes from background. Increased jet yields can help to explore higher multiplicity regions in 13 TeV analyses. Interestingly enough, the pseudorapidity of the $t\bar{t}Z$ system does not change. A further investigation and explanation of this phenomenon would be useful.

Apart from testing the $t\bar{t}Z$ modelling, also studies for signal and background discrimination have been performed. Artificial neural networks were trained to filter out $t\bar{t}V$ processes from the large abundance of $t\bar{t}$ background in the 2ℓOS channel. Simulations from the MC14 production campaign were used, which only provided a small number of events. A framework was developed to investigate the discrimination power of different network structures. Due to the low statistics, no significant results could be obtained. However, the established framework can prove useful for future efforts assisting to find a customised network structure.

Bibliography

[1] J. C. Street and E. C. Stevenson, *New Evidence for the Existence of a Particle of Mass Intermediate Between the Proton and Electron*, Phys. Rev. **52** (1937) 1003–1004.

[2] S. W. Herb et al., *Observation of a Dimuon Resonance at 9.5 GeV in 400-GeV Proton-Nucleus Collisions*, Phys. Rev. Lett. **39** (1977) 252–255.

[3] K.A. Olive et al. (Particle Data Group), *Review of Particle Physics*, Chin. Phys. C **38** (2014) 090001.

[4] ATLAS Collaboration, *Observation of a new particle in the search for the Standard Model Higgs boson with the ATLAS detector at the LHC*, Phys. Lett. B **716** (2012) no. 1, 1–29.

[5] CMS Collaboration, *Observation of a new boson at a mass of 125 GeV with the CMS experiment at the LHC*, Phys. Lett. B **716** (2012) no. 1, 30–61.

[6] P. W. Higgs, *Broken Symmetries and the Masses of Gauge Bosons*, Phys. Rev. Lett. **13** (1964) 508–509.

[7] F. Englert and R. Brout, *Broken Symmetry and the Mass of Gauge Vector Mesons*, Phys. Rev. Lett. **13** (1964) 321–323.

[8] M. Thomson, *Modern Particle Physics*. Cambridge University Press, 1st ed., 2013.

[9] Super-Kamiokande Collaboration, Y. Fukuda et al., *Evidence for Oscillation of Atmospheric Neutrinos*, Phys. Rev. Lett. **81** (1998) 1562–1567.

[10] SNO Collaboration, *Measurement of the Rate of* $\nu_e + d \rightarrow p + p + e^-$ *Interactions Produced by* ^{8}B *Solar Neutrinos at the Sudbury Neutrino Observatory*, Phys. Rev. Lett. **87** (2001) 071301.

[11] C.-S. Wu et al., *Experimental test of parity conservation in beta decay*, Phys. Rev. **105** (1957) no. 4, 1413.

[12] H. Frauenfelder et al., *Parity and the Polarization of Electrons from* Co^{60}, Phys. Rev. **106** (1957) 386–387.

[13] M. Goldhaber, L. Grodzins, and A. W. Sunyar, *Helicity of Neutrinos*, Phys. Rev. **109** (1958) 1015–1017.

[14] S. L. Glashow, *Partial-symmetries of weak interactions*, Nucl. Phys. **22** (1961) 579.

[15] S. Weinberg, *A model of leptons*, Phys. Rev. Lett. **19** (1967) no. 21, 1264.

[16] A. Salam, *Weak and Electromagnetic Interactions*, Conf. Proc. **C680519** (1968) 367–377. Reprinted in C.H. Lai., *Gauge Theory of Weak and Electromagnetic Interactions*. World Scientific Singapore, 1981.

[17] N. Cabibbo, *Unitary symmetry and leptonic decays*, Phys. Rev. Lett. **10** (1963) no. 12, 531.

[18] M. Kobayashi and T. Maskawa, *CP-violation in the renormalizable theory of weak interaction*, Prog. Theor. Phys. **49** (1973) no. 2, 652–657.

[19] CDF Collaboration, *Observation of Top Quark Production in* $\overline{p}p$ *Collisions with the Collider Detector at Fermilab*, Phys. Rev. Lett. **74** (1995) 2626–2631.

[20] D0 Collaboration, *Observation of the top quark*, Phys. Rev. Lett. **74** (1995) 2632–2637.

[21] M. L. Perl et al., *Evidence for Anomalous Lepton Production in* $e^+ - e^-$ *Annihilation*, Phys. Rev. Lett. **35** (1975) 1489–1492.

[22] ATLAS, CDF, CMS, D0, *First combination of Tevatron and LHC measurements of the top-quark mass*, ATLAS-CONF-2014-008, 2014.

[23] I. Bigi et al., *Production and decay properties of ultra-heavy quarks*, Phys. Lett. B **181** (1986) no. 1–2, 157 – 163.

[24] A. Quadt, *Top Quark Physics at Hadron Colliders*. Springer-Verlag Berlin Heidelberg, 2007. Originally published in Eur. Phys. J. C **48** (2006) 835-1000.

[25] H.-L. Lai et al., *New parton distributions for collider physics*, Phys. Rev. **D82** (2010) 074024.

[26] *The Durham HepData Project*, `http://hepdata.cedar.ac.uk/pdf/pdf3.html`.

[27] M. Czakon and A. Mitov, *Top++: A Program for the Calculation of the Top-Pair Cross-Section at Hadron Colliders*, Comput. Phys. Commun. **185** (2014) 2930.

[28] M. Aliev et al., *HATHOR: HAdronic Top and Heavy quarks crOss section calculatoR*, Comput. Phys. Commun. **182** (2011) 1034–1046.

[29] P. Kant et al., *HatHor for single top-quark production: Updated predictions and uncertainty estimates for single top-quark production in hadronic collisions*, Comput. Phys. Commun. **191** (2015) 74–89.

[30] F. Bezrukov and M. Shaposhnikov, *Why should we care about the top quark Yukawa coupling?*, J. Exp. Theor. Phys. **120** (2015) no. 3, 335–343.

[31] ATLAS Collaboration, *Measurement of the top quark charge in pp collisions at $\sqrt{s} = 7$ TeV with the ATLAS detector*, JHEP **11** (2013) 031.

[32] U. Baur, M. Buice, and L. H. Orr, *Direct measurement of the top quark charge at hadron colliders*, Phys. Rev. D **64** (2001) 094019.

[33] ATLAS Collaboration, *Observation of top-quark pair production in association with a photon and measurement of the $t\bar{t}\gamma$ production cross section in pp collisions at $\sqrt{s} = 7$ TeV using the ATLAS detector*, Phys. Rev. D **91** (2015) 072007.

[34] ATLAS Collaboration, *Search for single top-quark production via FCNC in strong interaction in $\sqrt{s} = 8$ TeV ATLAS data*, ATLAS-CONF-2013-063, Jul, 2013.

[35] D0 Collaboration, *Search for flavor changing neutral currents via quark–gluon couplings in single top quark production using 2.3 fb- 1 of collisions*, Phys. Lett. B **693** (2010) no. 2, 81–87.

[36] A. Czarnecki, J. G. Korner, and J. H. Piclum, *Helicity fractions of W bosons from top quark decays at NNLO in QCD*, Phys. Rev. D **81** (2010) 111503.

[37] ATLAS Collaboration, *Measurement of the W boson polarization in top quark decays with the ATLAS detector*, JHEP **06** (2012) 088.

[38] CMS Collaboration, *Measurement of the W-boson helicity in top-quark decays from $t\bar{t}$ production in lepton+jets events in pp collisions at $\sqrt{s} = 7$ TeV*, JHEP **10** (2013) 167.

[39] CMS Collaboration, *Search for flavor changing neutral currents in top quark decays in pp collisions at 8 TeV*, CMS-PAS-TOP-12-037, 2013.

[40] R. Röntsch and M. Schulze, *Probing top-Z dipole moments at the LHC and ILC*, JHEP **08** (2015) 044.

[41] R. Röntsch and M. Schulze, *Constraining couplings of top quarks to the Z boson in $t\bar{t}$ + Z production at the LHC*, JHEP **07** (2014) 091. Erratum: JHEP **09** (2015) 132.

[42] J. Alwall et al., *The automated computation of tree-level and next-to-leading order differential cross sections, and their matching to parton shower simulations*, JHEP **07** (2014) 079.

[43] F. Maltoni, D. Pagani, and I. Tsinikos, *Associated production of a top-quark pair with vector bosons at NLO in QCD: impact on $t\bar{t}H$ searches at the LHC*, JHEP **02** (2016) 113.

[44] S. Frixione et al., *Electroweak and QCD corrections to top-pair hadroproduction in association with heavy bosons*, JHEP **06** (2015) 184.

[45] J. M. Campbell and R. K. Ellis, *$t\bar{t}W^{+-}$ production and decay at NLO*, JHEP **07** (2012) 052.

[46] T. Gleisberg et al., *Event generation with SHERPA 1.1*, JHEP **02** (2009) 007.

[47] ATLAS Collaboration, *Search for $t\bar{t}Z$ production in the three lepton final state with 4.7 fb^{-1} of $\sqrt{s} = 7$ TeV pp collision data collected by the ATLAS detector*, ATLAS-CONF-2012-126, 2012.

[48] CMS Collaboration, *Measurement of associated production of vector bosons and top quark-antiquark pairs in pp collisions at $\sqrt{s}$=7 TeV*, Phys. Rev. Lett. **110** (2013) 172002.

[49] CMS Collaboration, *Measurement of top quark pair production in association with a W or Z boson using event reconstruction techniques*, CMS-PAS-TOP-14-021, 2015.

[50] ATLAS Collaboration, *Measurement of the $t\bar{t}W$ and $t\bar{t}Z$ production cross sections in pp collisions at $\sqrt{s} = 8$ TeV with the ATLAS detector*, ATLAS-CONF-2015-032, 2015.

[51] ATLAS Collaboration, *Measurement of the $t\bar{t}Z$ and $t\bar{t}W$ production cross sections in multilepton final states using 3.2 fb^{-1} of pp collisions at 13 TeV at the LHC*, ATLAS-CONF-2016-003, 2016.

[52] CMS Collaboration, *Measurement of the cross section of top quark pair production in association with a Z boson in pp collisions at 13 TeV*, CMS-PAS-TOP-16-009, 2016.

[53] A. Buckley et al., *General-purpose event generators for LHC physics*, Phys. Rept. **504** (2011) 145–233.

[54] T. Sjostrand, S. Mrenna, and P. Z. Skands, *PYTHIA 6.4 Physics and Manual*, JHEP **05** (2006) 026.

[55] T. Sjostrand, S. Mrenna, and P. Z. Skands, *A Brief Introduction to PYTHIA 8.1*, Comput. Phys. Commun. **178** (2008) 852–867.

[56] O. S. Brüning et al., *LHC Design Report*. CERN, 2004.

[57] ATLAS Collaboration, *ATLAS detector and physics performance: Technical Design Report, 1*. CERN, 1999.

[58] ATLAS Collaboration, *The ATLAS Experiment at the CERN Large Hadron Collider*, JINST **3** (2008) S08003.

[59] W. Panduro Vazquez on behalf of the ATLAS collaboration, *The ATLAS Data Acquisition System: from Run 1 to Run 2*, Nucl. Part. Phys. Proc. **273-275** (2014) 939–944.

[60] ATLAS Collaboration, *Modelling of the $t\bar{t}H$ and $t\bar{t}V$ $(V = W, Z)$ processes for $\sqrt{s} = 13$ TeV ATLAS analyses*, ATL-PHYS-PUB-2016-005, 2016.

[61] ATLAS Collaboration, *Validation of Monte Carlo event generators in the ATLAS Collaboration for LHC Run 2*, ATL-PHYS-PUB-2016-001, 2016.

[62] L. Lonnblad, *Correcting the color dipole cascade model with fixed order matrix elements*, JHEP **05** (2002) 046.

[63] L. Lonnblad and S. Prestel, *Matching Tree-Level Matrix Elements with Interleaved Showers*, JHEP **03** (2012) 019.

[64] R. D. Ball et al., *Parton distributions with LHC data*, Nucl. Phys. **B867** (2013) 244–289.

[65] ATLAS Collaboration, *ATLAS Run 1 Pythia8 tunes*, ATL-PHYS-PUB-2014-021.

[66] S. Hoeche et al., *QCD matrix elements and truncated showers*, JHEP **05** (2009) 053.

[67] P. Artoisenet et al., *Automatic spin-entangled decays of heavy resonances in Monte Carlo simulations*, JHEP **03** (2013) 015.

[68] M. Cacciari, G. P. Salam, and G. Soyez, *The Anti-k(t) jet clustering algorithm*, JHEP **04** (2008) 063.

[69] J. Pumplin et al., *New generation of parton distributions with uncertainties from global QCD analysis*, JHEP **07** (2002) 012.

[70] ATLAS Collaboration, *Measurements of spin correlation in top-antitop quark events from proton-proton collisions at $\sqrt{s} = 7$ TeV using the ATLAS detector*, Phys. Rev. **D90** (2014) no. 11, 112016.

[71] F. Hubaut et al., *ATLAS sensitivity to top quark and W boson polarization in $t\bar{t}$ events*, Eur. Phys. J. **C44S2** (2005) 13–33.

[72] A. Brandenburg, Z. G. Si, and P. Uwer, *QCD corrected spin analyzing power of jets in decays of polarized top quarks*, Phys. Lett. **B539** (2002) 235–241.

[73] W. Bernreuther and Z.-G. Si, *Top quark spin correlations and polarization at the LHC: standard model predictions and effects of anomalous top chromo moments*, Phys. Lett. **B725** (2013) 115–122. Erratum: Phys. Lett. B **744** (2015) 413.

[74] W. Bernreuther, A. Brandenburg, Z. G. Si, and P. Uwer, *Top quark pair production and decay at hadron colliders*, Nucl. Phys. **B690** (2004) 81–137.

[75] M. V. Garzelli et al., *$t\bar{t}W^{+-}$ and $t\bar{t}Z$ Hadroproduction at NLO accuracy in QCD with Parton Shower and Hadronization effects*, JHEP **11** (2012) 056.

[76] T. Vazquez Schroeder, *Measurement of the associated production of a vector boson (W, Z) and top quark pair in the opposite sign dilepton channel with pp collisions at $\sqrt{s} = 8$ TeV with the ATLAS detector*, II.Physik-UniGö-Diss-2014/06, 2014. PhD thesis, Göttingen University.

[77] W. Stauber, *Event classification for $t\bar{t}Z$ and $t\bar{t}W$ measurements using multivariate analyses*, II.Physik-UniGö-BSc-2015/06, 2015. BSc thesis, Göttingen University.

[78] O. Behnke et al., eds., *Data Analysis in High Energy Physics: A Practical Guide to Statistical Methods*. Wiley-VCH, 1 ed., 2013.

[79] C. M. Bishop, *Neural Networks for Pattern Recognition*. Clarendon Press, 1 ed., 1995.

[80] T. Hastie, R. Tibshirani, and J. Friedman, *The Elements of Statistical Learning: Data Mining, Inference, and Prediction, Second Edition*. Springer, 2nd ed., 4, 2011.

[81] A. Höcker et al., *TMVA - Toolkit for Multivariate Data Analysis*, CERN-OPEN-2007-007, 2007.

[82] G. Cybenko, *Approximation by superpositions of a sigmoidal function*, Math. Control. Signal. **2** no. 4, 303–314.

[83] A. R. Barron, *Universal approximation bounds for superpositions of a sigmoidal function*, IEEE T. Inform. Theory. **39** (1993) no. 3, 930–944.

[84] S. Alioli et al., *A general framework for implementing NLO calculations in shower Monte Carlo programs: the POWHEG BOX*, JHEP **06** (2010) 043.

[85] ATLAS Collaboration, *ATLAS tunes of PYTHIA 6 and Pythia 8 for MC11*, ATL-PHYS-PUB-2011-009, 2011.

[86] P. Z. Skands, *Tuning Monte Carlo Generators: The Perugia Tunes*, Phys. Rev. **D82** (2010) 074018.

A. Sherpa Simulations of $t\bar{t}Z$

To estimate the contribution of gluon fusion and quark-antiquark annihilation to $t\bar{t}Z$ production, a plain SHERPA simulation at LO was performed. The results are summarised in the following table.

The absolute cross sections are about 30% lower than in NLO computations. This is consistent with other simulations, for example Ref. [42]. The share of gluon fusion increases with the centre-of-mass energy, because of the high number of gluons at small momentum fractions x.

	8 TeV	13 TeV	14 TeV
Cross section with gg fusion	75.4 fb	367.4 fb	456.7 fb
Cross section with $q\bar{q}$ annihilation	71.8 fb	200.8 fb	230.0 fb
Contribution of gg fusion	51%	65%	67%
Contribution of $q\bar{q}$ annihilation	49%	35%	33%

Table A.1.: Contribution of gg fusion and $q\bar{q}$ annihilation to $t\bar{t}Z$ production. As renormalisation and factorisation scales $\mu_0^2 = (265\text{ GeV})^2 \approx (m_t + \frac{m_Z}{2})^2$ was used.

B. EVNT Files

All studies are based on datasets generated privately or within the MC validation effort. An overview of all samples presented in this thesis is given in the following referring to the `EVNT` files. Derived `xAODs` are produced with `TRUTH1` compression using the `AtlasDerivation 20.1.7.1` setup. These `DAODs` are then analysed for their particle content and kinematics with the `RootCore Base, 2.0.24` framework.

Setup at 8 TeV (Section 5.2.1)

`user.mcfayden.evnt.2015-05-07_025202.100000.8TeV_ttZllon_EXT1/`

`user.mcfayden.evnt.2015-05-07_025225.100001.8TeV_ttZllon_EXT1/`

`user.mcfayden.evnt.2015-05-20_103645.500000.8TeV_ttZllon_cteq6l1_EXT1/`

`user.mcfayden.evnt.2015-05-20_103709.500001.8TeV_ttZllon_cteq6l1_EXT1/`

Setup at 13 TeV (Section 5.2.2)

`mc15_valid.410073.MadGraphPythia8EvtGen_A14NNPDF23LO_ttZnnqq_Np0.evgen.EVNT.e4462/`

`mc15_valid.410073.MadGraphPythia8EvtGen_A14NNPDF23LO_ttZnnqq_Np0.evgen.EVNT.e4493/`

`mc15_13TeV.410073.MadGraphPythia8EvtGen_A14NNPDF23LO_ttZnnqq_Np0.evgen.EVNT.e4631/`

`mc15_13TeV.410074.MadGraphPythia8EvtGen_A14NNPDF23LO_ttZnnqq_Np1.evgen.EVNT.e4631/`

`mc15_13TeV.410075.MadGraphPythia8EvtGen_A14NNPDF23LO_ttZnnqq_Np2.evgen.EVNT.e4631/`

`mc15_13TeV.410143.Sherpa_NNPDF30NNLO_ttZnnqq.evgen.EVNT.e4686/`

`user.mcfayden.evnt.2015-08-14_111550.410002.13TeV_ttZqq_EXT1/`

Comparison of 8 TeV and 13 TeV (Section 5.2.3)

`user.mcfayden.evnt.2015-08-14_111550.410002.13TeV_ttZqq_EXT1/`

`user.mcfayden.evnt.2015-08-15_120852.410002.8TeV_ttZqq_EXT1/`

C. Variables for MVA

Variable	Definition
ΔR_{ave}^{jj}	$\Delta R(j,j)$ averaged for all jet pairs
H_T	Scalar sum of transverse momentum of final-state objects[1](charged leptons and jets)
$\mathrm{Cent}_{\mathrm{jet}}$	Scalar sum of p_T divided by sum of E for all jets
H1	Second Fox-Wolfram moment
$\mathrm{H1}_{\mathrm{jet}}$	Second Fox-Wolfram moment built from jets
max $M_{\ell\mathrm{b}}^{\mathrm{Min}\Delta\mathrm{R}}$	Maximum mass of a lepton ℓ and a b-tagged jet b with the smallest $\Delta R(\ell, b)$
$M_{jj}^{\mathrm{Min}\Delta\mathrm{R}}$	Mass of the two jets with smallest ΔR
$N_{\mathrm{jets}}^{\lvert M_{jj}-M(V)\rvert<30\ \mathrm{GeV}}$	Number of jet pairs with invariant di-jet mass in a window of 30 GeV around 85 GeV
N_{40}^{jet}	Number of jets with $p_T > 40$ GeV
M_{bb}^{MaxPt}	Mass of two b-tagged jets with the largest vector sum p_T
M_{bj}^{MaxPt}	Mass of one b-tagged and one arbitrary jet with the largest vector sum p_T
M_{jj}^{MaxPt}	Mass of two jets with the largest vector sum p_T
M_{uu}^{MaxPt}	Mass of two untagged jets with the largest vector sum p_T
$\Delta R_{\ell\ell}$	$\Delta R(\ell^+, \ell^-)$
$p_T^{\ell\ell,\mathrm{vec}}$	Vector sum of two leptons' transverse momenta
$p_T^{\ell\ell,\mathrm{vec}}/H_T^{\ell\ell}$	See above. Scalar sum of transverse lepton momenta
$\Delta R_{\mathrm{MaxPt}^{\mathrm{jj}}}$	ΔR of two jets with the highest p_T
Δw_{23}	Difference between second and third highest b-tagging weight

Table C.1.: Variables used for neural network training in section 6.3. They are taken from [76] and [77].

[1]Note that this definition is different from H_T as defined for the scale choice in MC generators.

Danksagung

Für das Gelingen einer wissenschaftlichen Arbeit ist man selbst verantwortlich – keine Frage. Aber wie würde diese Masterarbeit wohl aussehen, wenn ich keine dummen Fragen hätte stellen können, keine fachlichen Diskussionen geführt hätte oder keine kritische Rückmeldung erhalten hätte? Nicht so, auf jeden Fall. Für das vergangene Jahr am II. Institut möchte ich mich herzlich bedanken.

Ich bin Herrn Professor Quadt dankbar dafür, dass er mir die Möglichkeit gegeben hat, in seiner Arbeitsgruppe die Masterarbeit zu schreiben. Vielen Dank auch an Stan, dass er sich bereiterklärt hat, die Arbeit als Zweitkorrektor zu lesen. Boris stand mir während der gesamten Zeit hilfreich zur Seite und nahm sich immer Zeit für mich. Das ist viel wert! Ich konnte mich auch an Maria wenden, die mir bei Fragen zu Validierungsstudien weiterhalf, und an Nils, mit dem ich viel über multivariate Analysen diskutierte.

Abwechslungsreich war das fachlich bunt zusammengewürfelte Büro. Die konzentrierte Arbeitszeit, unterbrochen von amüsanten Unterhaltungen, LaTeX-Diskussionen oder PiA-Experimenten mit Julia, Enrico und Knut, habe ich sehr genossen. Vielen Dank für die gemeinsame Zeit!

Boris, Maria, Knut und Papa haben sich viel Zeit genommen, um meine Arbeit zu lesen und mir konstruktive Kritik zu geben. Danke!

Unzählige Pausen in der CaPhy habe ich mit Physikern eingelegt. Daneben haben uns die Uniliga mit dem FCC und die Skifahrten sportliche Abwechslung verschafft. Ablenkung vom Physikalltag hatte ich auch mit Bundesbrüdern auf dem Verbindungshaus bei und abseits von Veranstaltungen. Ebenso möchte ich die gemeinsamen Wochenenden und Hochzeiten mit der „krassen Herde“ nicht missen. Ihr habt mir alle abseits der Physik in Göttingen eine unvergessliche Zeit bereitet.

Ganz besonders möchte ich meiner Familie danken. Ihr habt mich das ganze Studium über unterstützt und mir bei wichtigen Entscheidungen zur Seite gestanden. Ich denke immer an die vielen schönen und lustigen Stunden mit euch, Mama, Papa, Dorothea, Johannes, Matthias!

Erklärung nach §17(9) der Prüfungsordnung für den Bachelor-Studiengang Physik und den Master-Studiengang Physik an der Universität Göttingen:

Hiermit erkläre ich, dass ich diese Abschlussarbeit selbständig verfasst habe, keine anderen als die angegebenen Quellen und Hilfsmittel benutzt habe und alle Stellen, die wörtlich oder sinngemäß aus veröffentlichten Schriften entnommen wurden, als solche kenntlich gemacht habe.
In Übereinstimmung mit gängiger Zitierpraxis ist allgemeines Wissen im Gebiet der Teilchenphysik, das Textbüchern entnommen werden kann, nicht zitiert. Ebenso sind für Abbildungen, die keine wissenschaftliche Leistung enthalten, keine Quellen angegeben.
Darüberhinaus erkläre ich, dass diese Abschlussarbeit nicht, auch nicht auszugsweise, im Rahmen einer nichtbestandenen Prüfung an dieser oder einer anderen Hochschule eingereicht wurde.

Göttingen, den 15. April 2016

(Konstantin Lehmann)